Cosmogenic and nucleogenic 21Ne in quartz in a 28-meter sandstone core from the McMurdo Dry Valleys, Antarctica

Greg Balco, Pierre-Henri Blard, D. L. Shuster, John H Stone, Laurent Zimmermann

Cosmogenic and nucleogenic ^{21}Ne in quartz in a 28-meter sandstone core from the McMurdo Dry Valleys, Antarctica

Greg Balco[*,a], Pierre-Henri Blard[b], David L. Shuster[d,a], John O.H. Stone[c], Laurent Zimmermann[b]

[a] *Berkeley Geochronology Center, 2455 Ridge Road, Berkeley CA 94709 USA*
[b] *CRPG, CNRS-Université de Lorraine, UMR 7358, 15 rue Notre Dame des Pauvres, 54501 Vandoeuvre-lès-Nancy, France*
[c] *Earth and Space Sciences, University of Washington, Seattle WA USA*
[d] *Department of Earth and Planetary Science, 479 McCone Hall, University of California, Berkeley CA 94720, USA*

Abstract

We measured concentrations of Ne isotopes in quartz in a 27.6-meter sandstone core from a low-erosion-rate site at 2183 m elevation at Beacon Heights in the Antarctic Dry Valleys. Surface concentrations of cosmogenic ^{21}Ne indicate a surface exposure age of at least 4.1 Ma and an erosion rate no higher than ca. 14 cm Myr^{-1}. ^{21}Ne concentrations in the upper few centimeters of the core show evidence for secondary spallogenic neutron escape effects at the rock surface, which is predicted by first-principles models of cosmogenic-nuclide production but is not commonly observed in natural examples. We used a model for ^{21}Ne production by various mechanisms fit to the observations to distinguish cosmic-ray-produced ^{21}Ne from nucleogenic ^{21}Ne produced by decay of trace U and Th present in quartz, and also constrain rates of subsurface ^{21}Ne production by cosmic-ray muons. Core samples have a quartz (U-Th)/Ne closure age, reflecting cooling below ~95°C, near 160 Ma, which is consistent with existing apatite fission-track data and the 183 Ma emplacement of nearby Ferrar dolerite intrusions. Constraints on ^{21}Ne production by muons derived from model fitting are consistent with a previously proposed value of 0.79 mb at 190 GeV for the cross-section for ^{21}Ne production by fast muon interactions, but indicate that ^{21}Ne production by negative muon capture is likely negligible.

Key words: neon-21, cosmogenic-nuclide geochemistry, (U-Th)/Ne thermochronology, McMurdo Dry Valleys, Antarctica

1. Introduction

This paper describes mass-spectrometric measurements of neon abundance and isotope composition in quartz in a sandstone bedrock core from the Antarctic Dry Valleys.

[*]Corresponding author. Tel. 510.644.9200 Fax 510.644.9201
Email address: balcs@bgc.org (Greg Balco)

The purpose of the measurements is to quantify the magnitude, relative importance, and depth-dependence of ^{21}Ne production in near-surface rocks due to cosmic-ray neutron spallation and cosmic-ray muon interactions. In addition, we quantify non-cosmogenic production of ^{21}Ne in quartz by alpha capture reactions due to decay of naturally occurring U and Th. This is important because cosmic-ray-produced ^{21}Ne is commonly used in a variety of applications in Earth surface processes research, including surface exposure dating, erosion rate estimation, and burial dating (see summary in Dunai, 2010), and these applications require accurate estimates of surface and subsurface production rates by these processes.

The various mechanisms for cosmogenic-nuclide production display different functional dependences on depth below the surface. Thus, by collecting samples at a range of depths where different production processes are dominant, one can quantify the relative magnitude of the different processes, and also obtain estimates for parameters such as attenuation thicknesses and interaction cross-sections that are necessary for production rate calculations. Cosmogenic ^{21}Ne, like other commonly measured cosmic-ray-produced nuclides (e.g., ^{10}Be or ^{26}Al), is produced at the Earth's surface primarily by spallation reactions induced by high-energy neutrons in the energy range 30 MeV - 1 GeV, the rate of which decreases exponentially with mass depth below the surface with an e-folding length in the range 140-160 g cm^{-2}. Production by weakly interacting muons is approximately two orders of magnitude less than spallogenic production at the surface, but decreases much more slowly with depth, so production below several meters depth is predominantly due to muons. In contrast to ^{10}Be and ^{26}Al, however, ^{21}Ne is also produced in significant quantities by capture of alpha particles derived from decay of naturally occurring U and Th in minerals via the reaction ^{18}O(α,n)^{21}Ne. Because ^{21}Ne is stable and has a geologic closure temperature in quartz of ~95°C (for 10°C/Myr cooling rate; see Shuster and Farley (2005)), quartz in rocks that reside near the surface for geologically long time periods accumulates significant quantities of nucleogenic ^{21}Ne via this process, and this can present an obstacle to accurately measuring the amount of cosmogenic ^{21}Ne. Given a series of subsurface ^{21}Ne measurements from a core, however, nucleogenic and cosmogenic ^{21}Ne can be distinguished because cosmogenic ^{21}Ne concentrations depend only on mass depth below the surface, whereas nucleogenic ^{21}Ne concentrations are not related to mass depth, but instead depend on the U and Th concentrations and closure age for the target mineral.

In the rest of this paper, we describe measurements of Ne isotopes in the core and related samples, and fit a forward model for nuclide concentrations to the core data. This allows us to (i) quantify the depth-dependence of near-surface spallogenic production; (ii) estimate the quartz (U-Th)/Ne closure age in sandstone bedrock at this site; (iii) show that there is no evidence for significant negative muon capture production of ^{21}Ne; and (iv) derive limits for the interaction cross-section for fast muon production of ^{21}Ne.

2. Analytical methods

2.1. The Beacon Heights sandstone core.

In January, 2009, a group associated with the "CRONUS-Earth" project and led by John Stone collected a 27.6-meter-long, 62mm diameter core of sandstone bedrock of

the Devonian Beacon Heights Orthoquartzite (McElroy and Rose, 1987) from a plateau at 77.85°S, 160.77°W and 2183 m elevation on University Peak, in the Beacon Heights region of the Quartermain Mountains, a subrange of the Transantarctic Mountains adjacent to the McMurdo Dry Valleys. The purpose of choosing this site is that surface erosion rates are in the range of cm/Myr, most likely close to the lowest observed anywhere on Earth, and geological evidence from the Dry Valleys region indicates that the site has most likely been continuously exposed at an extremely low erosion rate for perhaps as long as ~14.5 Ma (see Lewis et al., 2007, and references therein). Thus, cosmogenic-nuclide concentrations in surface bedrock at this site are extremely high, permitting accurate measurement, and the low erosion rate implies that concentrations of radionuclides such as ^{10}Be and ^{26}Al are likely close to equilibrium concentrations where production is balanced by radioactive decay, which facilitates production rate estimates for these nuclides (Borchers et al., 2016; Phillips et al., 2016; Balco, 2017). As we will discuss below, the advantage of high concentrations in estimating production rates applies to stable nuclides, but the equilibrium simplification does not.

Stone and co-workers at the University of Washington (UW) sectioned the core, measured the density of core segments, and supplied subsamples to a number of other laboratories for analysis. For this study, two laboratories (BGC and CRPG) made Ne isotope measurements on three lots of samples originally prepared in different laboratories (Table 1). A set of 20 samples was prepared at UW for ^{10}Be and ^{26}Al analysis by crushing, sieving to a grain size of 0.125-0.5 mm, etching in 1% HF at 50-70°C for at three periods of at least 24 hours, and sieving again to remove material less than 0.125 mm. Henceforth we refer to these samples as 'UW-sourced.' Aliquots of these etched samples were then provided to BGC for Ne analysis and measurement of U and Th concentrations. A different set of 3 samples ('Tulane-sourced') was prepared separately for analysis of in-situ-produced ^{14}C at Tulane University by crushing, sieving to a grain size of 0.25-0.5 mm, and etching in a 1% HF / 1% HNO_3 solution at 50°C for 2 24-hour periods. Aliquots of these etched samples were also provided to BGC. A final set of 11 samples ('CRPG-sourced') was prepared at CRPG by crushing core segments, sieving, and hand-picking of quartz grains. These were not HF-etched, and Ne and U/Th measurements were made at CRPG. Lastly, CRPG provided aliquots of three of the CRPG-sourced samples, as prepared for Ne measurements, to BGC for interlaboratory comparison purposes. These were analyzed at BGC as received from CRPG without further processing. Thus, 23 HF-etched core samples were analyzed only at BGC, 8 non-etched samples were analyzed only at CRPG, and 3 non-etched samples were analyzed at both BGC and CRPG. In addition, both laboratories analyzed the the CRONUS-A and CREU-1 (Jull et al., 2015; Vermeesch et al., 2015) quartz standards at the same time as core samples.

2.2. Holocene erratics of Beacon group sandstones from Mackay Glacier.

To further investigate nucleogenic ^{21}Ne concentrations in quartz in Beacon Group sandstones, we also made Ne measurements on a set of sandstone erratic clasts adjacent to Mackay Glacier, ca. 75 km north of the Beacon Heights core site. These samples are Beacon Group sandstones, although we do not know what stratigraphic level they originated at, that were collected for purposes of exposure-dating of Last Glacial Maximum-to-present ice sheet thinning by Jones et al. (2015) and are described in that

reference and also in Jones (2015). These samples are useful to us because they have Holocene ^{10}Be exposure ages that record the most recent deglaciation of the site, so we assume that they originated from subglacial erosion of fresh rock that has not previously been exposed at the surface, and have only experienced a single period of surface exposure during the Holocene. Thus, we can measure total excess ^{21}Ne concentrations in these samples and subtract cosmogenic ^{21}Ne concentrations calculated from ^{10}Be exposure ages to yield an estimate of nucleogenic ^{21}Ne. Quartz separates were prepared from these samples by Jones at Victoria University of Wellington by sieving to extract the 0.25-0.5 mm grain size fraction and etching in 5% HF for a total of 5 days. Aliquots of the same purified quartz separate used for ^{10}Be analysis were supplied to BGC for Ne analysis.

2.3. Neon measurements at BGC

All quartz samples received at BGC had already been purified by either HF-etching (UW-sourced, Tulane-sourced, and Mackay Glacier erratics) or hand-picking (CRPG-sourced), so we did not process them further before measurement. BGC has two noble gas analytical systems (the "MAP-II" and "Ohio" systems) that both consist of MAP-215 sector field mass spectrometers with modernized ion-counting electronics coupled to fully automated gas extraction systems. We used the MAP-II system for analysis of UW-sourced and CRPG-sourced core samples, and the Ohio system for later analysis of the Tulane-sourced core samples and the Mackay Glacier erratics.

Both systems employ a laser diode "microfurnace" heating system in which ca. 150 mg of quartz is encapsulated in a tantalum packet, and the packet is then heated with the laser under vacuum. An optical pyrometer is coaxial with the laser beam delivery optics, and laser and pyrometer are coupled to a Watlow PID controller, enabling the sample to be heated at a precisely controlled pyrometer temperature. The pyrometer temperature is calibrated for the emissivity of the Ta packet by heating a thermocouple in an identical apparatus; note, however, that precise temperature measurement is not relevant for this work. Analysis of each sample involved 2-4 heating steps with the final step at 1150-1200°C (see supplementary Table S1). In both systems, gas extracted from the sample by laser heating is reacted with one or more SAES getters and frozen to activated charcoal at 33 K. After pumping away non-adsorbed gases (presumably mostly helium in this case), neon is released into the mass spectrometer at 75 K.

In both systems, Ne signals are measured by ion counting using a Channeltron-type multiplier on masses 20, 21, and 22. Signals on masses 20 and 22 are corrected for $^{40}Ar^{++}$ and CO_2^{++}, respectively, using a ^{39}Ar spike as described in Balco and Shuster (2009). Absolute calibration of Ne abundance on both systems is made by peak height comparison against aliquots of an air standard containing between 5×10^{-16} and 2×10^{-14} mol Ne, processed in the same way as the samples and analyzed several times daily. Ne sensitivity was linear within this range at all times. Corrections for mass discrimination, when necessary, are also based on the air standard. Volume calibration of the pipette systems and measurement of the pressure of the air standards during loading employed several reference volumes and Baratron capacitance manometers, and the absolute calibration is completely independent between the two systems. As discussed below, measurements of the CRONUS-A and CREU-1 standards show that there is a measurable offset between the absolute calibration of the two systems.

2.4. Neon measurements at CRPG

At CRPG, individual quartz grains were selected from unprocessed crushed samples by hand-picking under a binocular microscope and cleaned in acetone in an ultrasonic bath for 10 minutes. They were then wrapped in 0.025 mm Cu foil (Alfa Aesar, 99.8% Cu) and placed under vacuum in a steel carousel that was then baked for 10 hours at 80°C. Neon was extracted in a custom-designed single vacuum resistance furnace equipped with a boron nitride crucible (Zimmermann et al., 2012). Most samples were heated in two 25-minute heating steps at 400°and 1250°C, followed by a final step at 1250-1300°C to ensure complete extraction (see supplementary Table S2). Released gases were exposed to activated charcoal cooled to liquid nitrogen temperature, titanium sponges (Johnson Matthey mesh m3N8/t2N8) and SAES getters (ST172/HI/20-10/650C). Ne and He were not separated and both were introduced into a VG5400 mass spectrometer. Three Ne isotopes were measured using an electron multiplier and Ortec ion counter. Isobaric interferences of $^{40}Ar^{++}$ on mass 20 and CO_2^{++} on mass 22 were found to be negligible compared to the total amount of Ne present. The mass spectrometer sensitivity was determined by peak height comparison against a Ne standard containing 2.7×10^{-14} mol ^{20}Ne and atmospheric Ne isotope composition, and found to be linear within the range of Ne pressures observed in sample measurements. Furnace blanks at 1000-1300°C for 25 minutes were $(2.1\pm0.1)\times10^{-16}$, $(5.4\pm0.1)\times10^{-19}$, and $(4.2\pm0.2)\times10^{-17}$ mol ^{20}Ne, ^{21}Ne, and ^{22}Ne respectively.

2.5. U and Th measurements at BGC and Caltech

We measured U and Th concentrations in aliquots of the same purified quartz used for Ne measurements by isotope dilution mass spectrometry (Tables 1,2; supplementary Table S4). Initially, we analyzed very small (3-6 mg) aliquots of the prepared quartz at Caltech using a procedure developed for single grain (U-Th)/He chronometry (House et al., 2000), in which the sample is spiked with a mixed ^{235}U - ^{230}Th spike, dissolved in concentrated HF, evaporated to dryness, and redissolved in a dilute HNO_3 solution for measurement of U and Th isotope ratios by ICP-MS. Although nominal uncertainties in the resulting concentrations derived from the precision of the isotope ratio measurements are less than 1%, U concentrations in replicates of some samples differed by up to 35%, and Th concentrations by up to 60%. We attributed this to a nugget effect caused by inhomogeneity of detrital quartz grains in the sandstone combined with the small sample size, so we then analyzed much larger aliquots (100-300 mg) of UW-sourced and Tulane-sourced samples, as well as the Mackay Glacier erratics, at BGC. We used a similar procedure in which we dissolved the quartz in concentrated HF, evaporated SiF_4 to remove Si, redissolved remaining trace elements in a dilute HNO_3 - trace HF mixture, spiked a subsample of this solution with a mixed ^{233}U - ^{229}Th spike, and measured U and Th isotope ratios in the spiked subsample using a Thermo Neptune ICP-MS. Although we cannot internally verify quantitative recovery of U and Th after sample drydown using this procedure, experiments with a normal solution containing known U and Th concentrations indicated complete recovery.

Replicate measurements on large aliquots also showed large differences in U and Th concentrations (see supplementary Table S4). This is consistent with the idea that significant fractions of U and Th in these samples may be concentrated in rare individual grains, perhaps containing refractory mineral inclusions or diagenetic cements, but

also shows that the effect is not mitigated by increasing the sample size. We hypothesize that this effect may be characteristic of detrital sandstones containing quartz grains with a diverse provenance, and might not be observed in quartz in igneous or metamorphic rocks. Regardless, it is clear that the actual reproducibility of these measurements is much less precise than the nominal measurement uncertainties for each aliquot, so we have disregarded the nominal measurement uncertainties. In Tables 1 and 2, we show average U and Th concentrations for all aliquots analysed for each sample, regardless of aliquot size. Given the available data and lacking a complete explanation for excess scatter, the true measurement uncertainty for U and Th measurements is most likely best approximated by the average standard deviation of replicate measurements on samples that were analyzed multiple times, which is is 17% for U and 27% for Th. We revisit this issue later in the model-fitting section.

2.6. U and Th measurements at CRPG

U and Th concentrations in CRPG-sourced quartz samples were measured using the standard procedure at the Service d'Analyse des Roches et des Minraux (SARM-CRPG), which consists of $LiBO_2$ fusion, dissolution of the fusion residue, and ICPMS measurement of U and Th concentration by peak height comparison with a standard.

2.7. Calculation of excess ^{21}Ne

Neon in natural quartz is typically a mixture of (i) "trapped" neon with atmospheric isotope composition, (ii) cosmogenic neon, and (iii) nucleogenic ^{21}Ne and ^{22}Ne derived from alpha capture reactions on ^{18}O and ^{19}F, respectively (Niedermann et al., 1993; Niedermann, 2002). In rare cases an additional "trapped" component with non-atmospheric isotope ratios is also present (e.g., Hetzel et al., 2002). Even in typical cases where the trapped component has atmospheric composition, it is generally not possible to accurately perform a three-component deconvolution from measurements of three isotopes, because (i) the relative abundance of O and F, and thus the isotope composition of the nucleogenic end member, are unlikely to be known, and (ii) nucleogenic neon is typically a minor component that is present at the level of analytical precision in the total neon concentration measurement, so it cannot be deconvolved precisely. In this work, we found no evidence for a non-atmospheric trapped component (see discussion below), so we assume that neon in all samples consists of a three-component mixture of atmospheric, cosmogenic, and nucleogenic neon. Commonly, one would estimate cosmogenic ^{21}Ne concentrations in this situation by assuming that nucleogenic ^{21}Ne is negligible, assuming that the sample is a two-component mixture of atmospheric and cosmogenic ^{21}Ne, and computing the cosmogenic ^{21}Ne concentration by a two-component deconvolution based on the ^{21}Ne/^{20}Ne ratio. However, as we show below, nucleogenic ^{21}Ne concentrations are significant in many of our samples, so we did not use this procedure and for each analysis we computed excess ^{21}Ne with respect to atmospheric composition ($N_{21,xs}$) as:

$$N_{21,xs} = N_{21,m} - R_{2120,a} N_{20,m} \tag{1}$$

where $N_{21,m}$ is the total amount of ^{21}Ne released in an analysis, $N_{20,m}$ is the total amount of ^{20}Ne released in an analysis, and $R_{2120,a}$ is the ^{21}Ne/^{20}Ne ratio in the atmosphere, which we take to be 0.002959. This formula can be derived by assuming that

the amount of cosmogenic ^{20}Ne is negligible in comparison to the amount of ^{20}Ne contributed by atmospheric neon. In this formulation $N_{21,m}$, $N_{20,m}$, and $N_{21,xs}$ could either pertain to a number of atoms (e.g., units of mol) or a concentration (mol g^{-1} or atoms g^{-1}).

Excess ^{21}Ne computed in this way includes both cosmogenic and nucleogenic ^{21}Ne. In subsequent sections we differentiate these two components by fitting a forward model for nucleogenic and cosmic-ray production of ^{21}Ne to the data. For completeness, note that we assume that no cosmogenic ^{21}Ne from initial exposure during sandstone deposition in the Devonian is present; any such ^{21}Ne inventory that may have existed is expected to have been lost during reheating associated with emplacement of 183 Ma Ferrar Dolerite intrusions (see additional discussion below).

3. Results

3.1. Neon isotope ratios

Complete three-isotope results of step-degassing neon measurements are shown in the supplementary material. Neon isotope ratios in all analyses were indistinguishable from a two-component mixing line between cosmogenic and atmospheric Ne. This agrees with many previous neon measurements in quartz from Beacon Group sandstones (Summerfield et al., 1999; Balco and Shuster, 2009; Balco et al., 2014; Middleton et al., 2012; Vermeesch et al., 2015). Although we will show later that cosmogenic neon is nearly negligible in the Mackay Glacier erratics as well as some samples from deep in the core, and therefore neon in these samples must contain only atmospheric and nucleogenic components, we did not find that neon isotope ratios in these samples were distinguishable from the atmospheric-cosmogenic mixing line. Primarily this is because the precision of ^{22}Ne measurements is insufficient to distinguish nucleogenic from cosmogenic ^{21}Ne enrichments in the presence of much larger amounts of atmospheric Ne (also see discussion in Middleton et al., 2012). In addition, it is possible that nucleogenic ^{22}Ne as well as ^{21}Ne is present, which could make it impossible to distinguish nucleogenic from cosmogenic ^{21}Ne excesses no matter what the ^{22}Ne measurement precision. Thus, as noted above, we have not attempted to differentiate nucleogenic and cosmogenic ^{21}Ne using the isotope ratio data alone, but instead compute excess ^{21}Ne with respect to atmospheric composition and then resolve this quantity into nucleogenic and cosmogenic contributions by considering the production systematics of both.

The proportion of total neon attributable to trapped Ne with atmospheric composition varies systematically between groups of samples prepared in different laboratories. CRPG-sourced samples, that were not HF-etched, had 124 ± 30 Matoms g^{-1} (mean and standard deviation of 11 samples) ^{21}Ne attributable to atmospheric Ne. UW-sourced samples that were repeatedly HF-etched to achieve low Al concentrations necessary for ^{26}Al measurement had 49 ± 11 Matoms g^{-1} (n = 20). This suggests that trapped atmospheric Ne is preferentially located in grain coatings or in secondary diagenetic silica cement, both of which would be removed during HF etching, rather than in quartz grains itself. However, Tulane-sourced samples and Mackay Glacier erratics, that were also HF-etched, had intermediate values of 105 ± 18 (n = 3) and 136 ± 44 (n = 13)

Matoms g^{-1}, respectively, which may instead indicate a grain-size dependence: UW-sourced samples were derived from finer grain-size fractions of crushed rock.

On the other hand, there is no evidence that sample pretreatment affected cosmogenic ^{21}Ne concentrations. No such effect is expected, because measurements of Ne diffusion kinetics in quartz (Shuster and Farley, 2005) do not predict significant diffusive Ne loss from heating to ~ 50°-70°C for several days during quartz etching. As we show later, differences in excess ^{21}Ne between differently-treated sample lots can be fully accounted for by differences in nucleogenic Ne concentrations that arise from corresponding differences in U and Th concentrations.

3.2. Normalization between analytical systems

Measurements of the CRONUS-A and CREU-1 quartz standards showed that the three noble gas analytical systems used for this work had significant differences in absolute calibration. Measurements of these standards at CRPG and on the BGC MAP-II system during the period of the Beacon Heights core measurements are described in Vermeesch et al. (2015) and show an offset of 13% between the two systems. Later measurements of the CRONUS-A standard on the BGC Ohio system run at the same time as core samples yielded a concentration of 319.0 ± 1.7 Matoms g^{-1} (error-weighted mean and standard error of 15 measurements), and a different set of measurements run at the same time as the Mackay Glacier samples yielded 320.1 ± 6.8 Matoms g^{-1} (error-weighted mean and standard error of 15 measurements) , which agree with the consensus value for this standard given by Vermeesch et al. (2015), but differ from results obtained on both the CRPG and BGC MAP-II systems. In addition, as noted above, we performed replicate analyses of three core samples on the CRPG and BGC MAP-II systems, and the results of these replicates were consistent with the offset derived from the CRONUS-A and CREU-1 standards (Figure 1). To obtain an internally consistent set of excess ^{21}Ne concentrations for subsequent analysis, therefore, we assumed that the offsets in replicate measurements between analytical systems reflect differences in the absolute calibration of the primary gas standards used for sensitivity calibration on each system, and renormalized all data to reference values for excess ^{21}Ne concentrations given by Vermeesch et al. (2015) for CREU-1 and CRONUS-A of 348 and 320 Matoms g^{-1}, respectively, using the following procedure. First, we renormalized CRPG data to be consistent with BGC MAP-II data using the error-weighted mean of the offsets of all replicate data shown in Figure 1, which is 1.122. Second, we then renormalized the resulting combined data set to a reference value for CRONUS-A of 320 Matoms g^{-1} using a correction factor of 0.944, which is based on a data set of 21 analyses of CRONUS-A performed on the BGC MAP-II system around the time the core samples were analysed, including the measurements reported in Vermeesch et al. (2015) as well as others. Third, measurements of CRONUS-A on the BGC Ohio system were indistinguishable from the reference value of 320 Matoms g^{-1}, so measurements on this system were not renormalized. We propose that the result of this procedure is an internally consistent set of measurements of excess ^{21}Ne referenced to the summary values of CRONUS-A and CREU-1 proposed by Vermeesch et al. (2015). Note that we did not apply uncertainties in the correction factors to compute expanded measurement uncertainties for each sample in the intercalibrated data set, because if

we did this, we would no longer be able to treat measurement uncertainties as independent between samples, which would complicate the model fitting exercises we describe later.

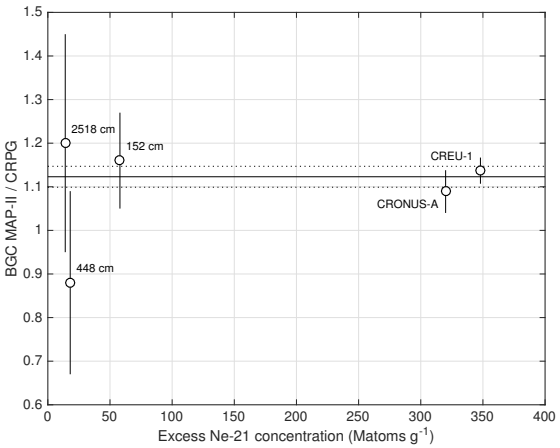

Figure 1: Offset between excess ^{21}Ne concentrations as measured on BGC MAP-II and CRPG systems for the CRONUS-A and CREU-1 standards and three core samples analysed on both systems. The y-axis is the ratio of the excess ^{21}Ne concentration as measured on the BGC MAP-II system to that measured on the CRPG system. Horizontal line shows the error-weighted mean of these data (1.123) used to normalize data from these systems to each other as well as the corresponding standard error (0.024). The reduced χ^2 statistic with respect to the error-weighted mean is 0.6.

3.3. Basic observations

Figure 2 shows excess ^{21}Ne concentrations in the core, normalized to standard reference values as described above, as well as U and Th concentrations. In this section, we highlight several important aspects of the results that we will seek to explain in detail in subsequent sections.

3.3.1. Nucleogenic ^{21}Ne in shielded samples

Figure 3 shows the relationship between excess ^{21}Ne and eU in samples deeper than 1000 g cm^{-2} in the core, where cosmic-ray production is expected to be minimal. eU approximates total alpha particle production from U and Th decay and is defined as ([U] + 0.235[Th]), where [U] and [Th] are U and Th concentrations in ppm. This relationship highlights two observations. First, U, Th, and ^{21}Ne concentrations are systematically lower in UW- and Tulane-sourced quartz samples, which were prepared by HF-etching, than in CRPG-sourced samples, which were not HF-etched (also see Figure 2). This indicates that in this lithology U and Th concentrations are higher in secondary grain coatings or diagenetic silica cement, that were presumably preferentially removed by HF etching, than in the interior of the quartz grains themselves. This is not surprising if U and Th are associated with trace clays or oxide minerals that are

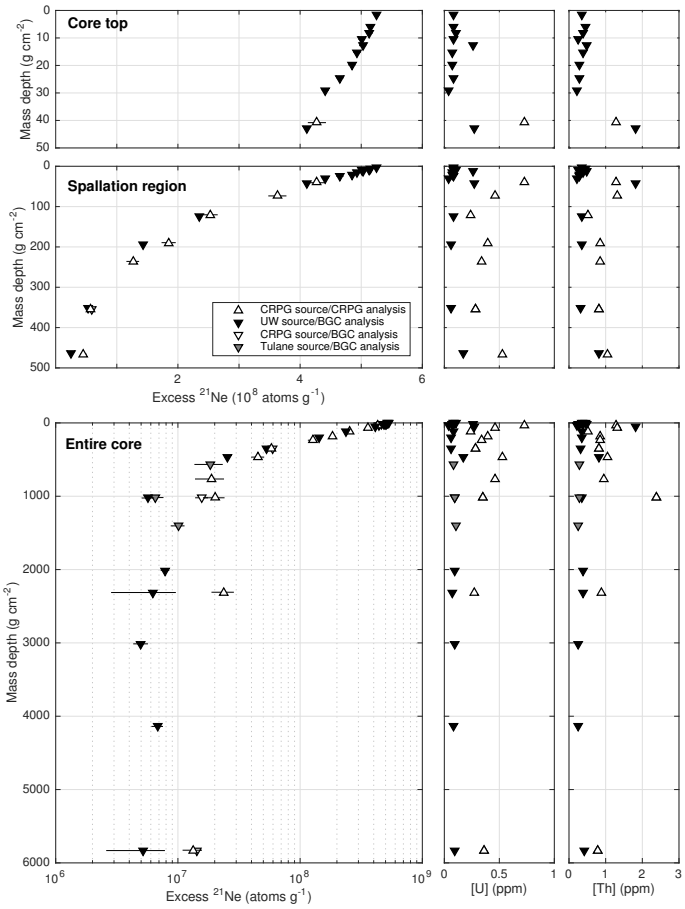

Figure 2: Excess ^{21}Ne concentrations (left panels) and U and Th concentrations (right panels) in quartz samples from the Beacon Heights core. The data are the same in all three sets of panels, but the axes are different so as to adequately show details in all parts of the core. Symbol shading denotes the sample lots: black, UW-sourced, white, CRPG-sourced, and gray, Tulane-sourced. Symbol shape denotes the location of the analysis: upward-pointing triangle, CRPG; downward-pointing, BGC.

present as contaminants in diagenetic silica cement. Second, eU is correlated with excess ^{21}Ne in the shielded part of the core ($p = 0.004$). Although presumably some nonzero fraction of measured excess ^{21}Ne in deep core samples is cosmogenic, this correlation indicates that the majority of excess ^{21}Ne in these samples is nucleogenic rather than cosmogenic.

Figure 3 also shows the relationship between eU and nucleogenic ^{21}Ne in the Mackay Glacier erratic samples. Table 2 shows the calculation of nucleogenic ^{21}Ne in these samples: we computed cosmogenic ^{21}Ne from measured ^{10}Be concentrations by assuming an ^{21}Ne/^{10}Be production ratio of 4 (see discussion below), then subtracted this from the observed excess ^{21}Ne concentration to yield an estimate of nucleogenic ^{21}Ne. eU and nucleogenic ^{21}Ne in these samples are correlated ($p = 0.07$), as expected if we have correctly estimated nucleogenic ^{21}Ne, U, and Th concentrations, and are consistent with the deep core samples. This also suggests that excess ^{21}Ne in deep core samples is predominantly nucleogenic.

Table 2 also shows calculated Ne closure ages (using Equation 3 below) for the Mackay Glacier erratics; these are scattered between 135-351 Ma with mean and standard deviation 233 ± 62 Ma. If we assume, as discussed above, that typical uncertainties in U and Th concentrations are ~20% and ~30%, respectively, this implies a total uncertainty in alpha particle production and thus in closure age estimates of ~20-25%. A 25% uncertainty on each age would imply reduced $\chi^2 = 1.1$ with respect to the mean, indicating that these estimates of closure age are imprecise but at least internally consistent. As discussed in more detail below, we expect the Ne closure age of Beacon Group sandstones to be similar to or less than the 183 Ma age of Ferrar dolerite intrusions that are pervasive within Beacon Group sandstones in the Dry Valleys (Bernet and Gaupp, 2005; Burgess et al., 2015), and these closure ages, although imprecise, are consistent with this hypothesis.

3.3.2. Limited muon-produced inventory

An additional implication of the correlation between eU and excess ^{21}Ne in shown in Figure 3 is that only a small fraction of excess ^{21}Ne observed in the core below 1000 g cm^{-2} is cosmogenic; if excess ^{21}Ne was predominantly cosmogenic, we would expect weak or no correlation with eU. Thus, the concentration of muon-produced ^{21}Ne is much smaller than that of nucleogenic ^{21}Ne. This potentially makes it difficult to accurately infer production rates due to muons from these data.

3.3.3. Surface fast neutron albedo effect

Figure 4 shows that nuclide concentrations near the bedrock surface diverge from the exponential relationship expected for spallogenic production. Presumably, this is due to a secondary particle escape or "albedo" effect that arises from the fact that the mean atomic weight of nuclei in rock is greater than that in air, so production of secondary neutrons with energies sufficient to induce ^{21}Ne production by Si spallation is higher in rock than in air. Thus, the gradient in neutron density at the surface results in "escape" of some neutrons from rock into air, and a corresponding reduction in ^{21}Ne production at the surface. This effect is predicted by first-principles particle transport models of cosmic-ray interactions with the Earth that aim to simulate cosmogenic-nuclide production (Masarik and Reedy, 1995; Masarik and Wieler, 2003; Argento

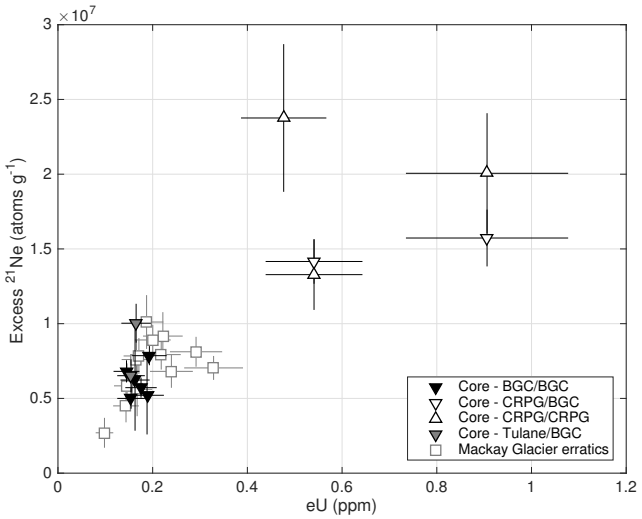

Figure 3: Relationship between eU and excess ^{21}Ne in samples deeper than 1000 g cm^{-2} in the core and between eU and nucleogenic ^{21}Ne in Mackay Glacier erratics. The symbols for core samples are the same as in Figure 2. Both eU and excess ^{21}Ne concentrations are significantly higher in CRPG-sourced samples that were not HF-etched. Error bars show measurement uncertainties for ^{21}Ne concentrations and an assumed 20% uncertainty in eU (see text).

et al., 2013). However, it is not generally observed in actual data sets of cosmogenic-nuclide measurements, presumably because one would only expect to observe it where (i) the surface erosion rate is low enough to prevent advection of rock from below through the thin near-surface zone where this effect is important, and (ii) nuclide concentrations are high enough that small deviations from an exponential relationship can be accurately measured. To our knowledge, the only other data set that shows this effect is the ^{26}Al measurements from the same core (Borchers et al., 2016; Phillips et al., 2016).

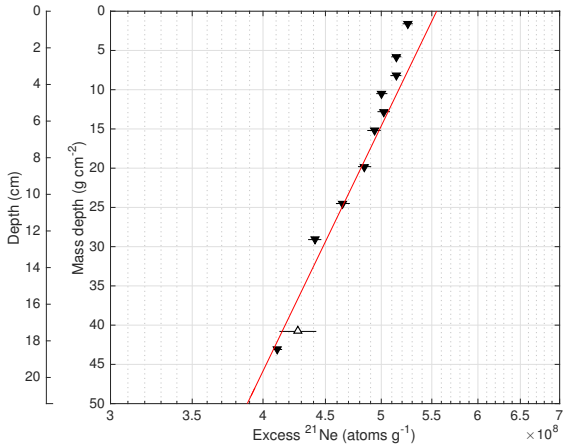

Figure 4: Excess ^{21}Ne in the uppermost 50 g cm^{-2} of the core compared to a representative simple exponential depth dependence with an e-folding length of 140 g cm^{-2}. Concentrations systematically diverge from an exponential relationship in the upper ca. 20 g cm^{-2}. In this plot, excess ^{21}Ne concentrations have not been corrected for variable amounts of nucleogenic ^{21}Ne resulting from varying [U] and [Th], so show more scatter than would be present for cosmogenic ^{21}Ne alone. We discuss this in more detail in the model fitting section below.

3.3.4. Comparison to ^{10}Be and ^{26}Al concentrations

Borchers et al. (2016) as well as Balco (2017) estimated muon interaction cross-sections for ^{10}Be and ^{26}Al production by fitting a production model to ^{10}Be and ^{26}Al concentrations in the Beacon Heights core under the assumption that ^{10}Be and ^{26}Al concentrations had reached equilbrium with steady erosion, that is, the surface had been steadily eroding at the same rate for a duration of at least several half-lives of these nuclides. However, surface ^{21}Ne concentrations at the site are not consistent with this assumption. Figure 5 shows surface ^{10}Be, ^{26}Al, and ^{21}Ne concentrations compared to predicted concentrations for a single period of exposure with zero erosion (the "simple exposure line") and steady erosion for a long enough period for surface nuclide concentrations to reach equilibrium between production and loss by radioactive decay (for radionuclides) and surface erosion (the "steady erosion line"). Although the ^{26}Al-^{10}Be pair is consistent with equilibrium steady erosion, ^{21}Ne concentrations are

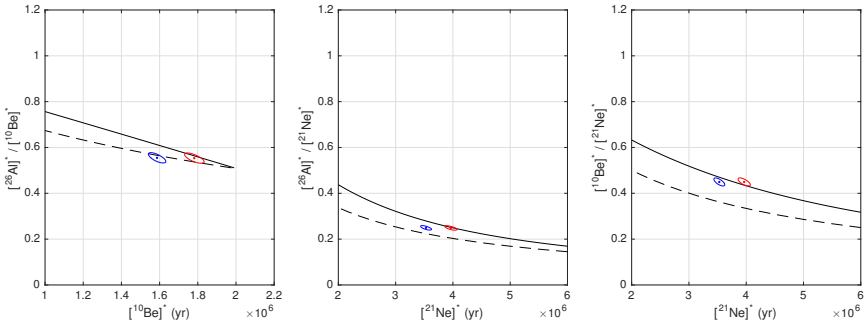

Figure 5: Paired nuclide diagrams for normalized ^{10}Be, ^{26}Al, and ^{21}Ne concentrations in the core surface sample. ^{10}Be and ^{26}Al concentrations are from Borchers et al. (2016). In all diagrams, the solid black line is the simple exposure line and the dashed black line is the steady erosion line. Red and blue ellipses show normalized nuclide concentrations predicted by the Antarctic atmosphere model of Stone (2000) and production rate scaling methods of Stone (2000) and Lifton et al. (2014), respectively, as implemented in version 3 of the online exposure age calculators described by Balco et al. (2008) and subsequently updated. We assumed that the ^{21}Ne/^{10}Be production ratio is 4.0 for both scaling methods (Balco and Shuster, 2009; Kober et al., 2008; Amidon et al., 2009; Kober et al., 2011).

not. In contrast, ^{21}Ne-^{26}Al and ^{21}Ne-^{10}Be pairs are better predicted by simple exposure at negligible erosion. This is not unexpected, because ^{21}Ne is not radioactive, so it requires a much longer time to reach production-erosion equilibrium than radionuclides would require to reach production-decay-erosion equilibrium. This comparison is somewhat complicated by the facts that our assumed surface production ratios (i) do not take account of fast neutron albedo effects discussed above, and (ii) are based on some studies (e.g., Balco and Shuster, 2009) that estimated the ^{21}Ne/^{10}Be production ratio by using assumptions about muon production that we will show to be incorrect. However, these effects are much smaller than the difference in predicted ^{21}Ne concentrations for steady-erosion and simple-exposure end members, so they do not affect the overall conclusion. In any case, this comparison indicates, as expected, that we cannot take advantage of the assumption that surface nuclide concentrations have reached production-erosion steady state to estimate ^{21}Ne production rates at this site. It also indicates that the use of this assumption by Borchers et al. (2016) and Balco (2017) may have caused them to slightly underestimate ^{26}Al and ^{10}Be production rates due to negative muon capture, although this effect is likely to be small.

4. Model fitting

In this section we formulate a forward model for excess ^{21}Ne concentrations in core samples and attempt to use it to constrain several unknown parameters in the model that are related to nucleogenic and muon-induced ^{21}Ne production.

Measured excess ^{21}Ne as calculated with Equation 1 includes nucleogenic ^{21}Ne as well as cosmogenic ^{21}Ne produced by cosmic-ray neutron spallation and muon interactions, as follows:

$$N_{21,xs} = N_{21,nuc} + N_{21,sp} + N_{21,\mu-} + N_{21,\mu f} \quad (2)$$

$N_{21,xs}$ (atoms g^{-1}) is excess ^{21}Ne, $N_{21,nuc}$ (atoms g^{-1}) is nucleogenic ^{21}Ne, $N_{21,sp}$ (atoms g^{-1}) is ^{21}Ne produced by high-energy neutron spallation, $N_{21,\mu-}$ (atoms g^{-1}) is ^{21}Ne produced by negative muon capture, and $N_{21,\mu f}$ (atoms g^{-1}) is ^{21}Ne produced by fast muon interactions.

Nucleogenic ^{21}Ne due to U and Th decay is:

$$N_{21,nuc} = \sum_i f_i F_{T,i} Y_{\alpha,i} N_i \left(e^{\lambda_i t_c} - 1\right) \quad (3)$$

where the index i refers to each radionuclide that acts as an alpha particle source, including ^{232}Th, ^{235}U, and ^{238}U. We disregard ^{147}Sm as insignificant. N_i is the concentration (atoms g^{-1}) of nuclide i, λ_i is the decay constant of nuclide i (yr^{-1}), $Y_{\alpha,i}$ is the yield of alpha particles throughout the decay chain of nuclide i ($Y_{\alpha,232} = 6$; $Y_{\alpha,235} = 7$, and $Y_{\alpha,238} = 8$; we assume secular equilibrium for each decay chain), f_i is the fraction of alpha particles produced from decay of nuclide i that react with ^{18}O to produce ^{21}Ne; and t_c is a neon closure age (yr), which represents the time at which the mineral cooled sufficiently to retain ^{21}Ne. The fractions f_i for quartz are given by Cox et al. (2015) and are $f_{232} = 6.08 \times 10^{-8}$; $f_{235} = 5.62 \times 10^{-8}$; and $f_{238} = 4.04 \times 10^{-8}$. We discuss the factor $F_{T,i}$ in the next paragraph, leaving the neon closure age t_C as the only unknown parameter in this formula.

$F_{T,i}$ is a factor that describes the fraction of alpha particles that are ejected at grain boundaries and thus cannot induce reactions within the grain (Farley et al., 1996). For samples that were prepared by HF etching, alpha-depleted grain boundaries have presumably been removed and $F_{T,i} = 1$ always. For CRPG-sourced samples that were not HF-etched, this is not the case, but the observation that bulk U and Th concentrations decrease substantially with etching indicates that U and Th are concentrated near grain boundaries, which violates the assumption of uniform U and Th distribution needed to compute $F_{T,i}$ in the usual fashion. To address this, we observe that mean eU in un-etched, CRPG-sourced samples is 2.8 times mean eU in etched samples. If we assume that the U and Th removed by etching is located exactly at the grain boundary, then 64% of eU is concentrated at the grain boundary. We can coarsely approximate F_T as a single, non-nuclide-dependent value for total alpha production by observing that if 64% of eU is concentrated at the grain boundary, and by definition half of alpha particles produced at the grain boundary are not implanted within the grain, then $F_T = (1 - (0.64/2)) = 0.68$. Although this approximation is speculative, it is consistent with the data shown in Figure 3 in that for these data the observed mean ratio of excess ^{21}Ne to eU in unetched, CRPG-sourced samples is less than that in HF-etched samples. To summarize, we assume for all i that $F_{T,i} = 1$ for etched samples and $F_{T,i} = 0.68$ for un-etched samples.

The remainder of the terms in Equation 2 describe cosmogenic ^{21}Ne. Cosmogenic-nuclide production due to fast neutron spallation is, in nearly all other work (e.g., Lal, 1988), assumed to decrease exponentially with mass depth below the surface such that:

$$P_{21,sp}(z) = P_{21,sp}(0) e^{-\frac{z}{\Lambda_{sp}}} \quad (4)$$

where z is mass depth below the surface (g cm^{-2}), $P_{21,sp}(z)$ is the ^{21}Ne production rate due to spallation (atoms g^{-1} yr^{-1}) at depth z, $P_{21,sp}(0)$ is the surface ^{21}Ne production rate due to spallation (atoms g^{-1} yr^{-1}), and Λ_{sp} is an effective e-folding length for spallogenic production (g cm^{-2}). However, in our data set, the evidence for near-surface secondary particle escape effects shown in Figure 4 means that a single-exponential formula is not adequate. Because we do not have a first-principles estimate of the exact form of the depth-dependence of the production rate due to this effect, we approximate it by assuming:

$$P_{21,sp}(z) = P_{21,sp}(0)e^{-\frac{z}{\Lambda_{sp}}} - P_{21,sp}(0)f_a e^{-\frac{z}{\Lambda_a}} \quad (5)$$

where fa (dimensionless) and Λ_a (g cm^{-2}) account for near-surface escape losses (e.g., see Phillips et al., 2001).

With this approximation, spallogenic ^{21}Ne as a function of mass depth z is:

$$N_{21,sp}(z) = P_{21,sp}(0)\int_0^t e^{-\frac{z+\epsilon\tau}{\Lambda_{sp}}}d\tau - P_{21,sp}(0)f_a\int_0^t e^{-\frac{z+\epsilon\tau}{\Lambda_a}}d\tau \quad (6)$$

$$N_{21,sp}(z) = \frac{P_{21,sp}(0)e^{-\frac{z}{\Lambda_{sp}}}\Lambda_{sp}}{\epsilon}\left(1 - e^{-\frac{\epsilon}{\Lambda_{sp}}t}\right) - \frac{P_{21,sp}(0)f_a e^{-\frac{z}{\Lambda_a}}\Lambda_a}{\epsilon}\left(1 - e^{-\frac{\epsilon}{\Lambda_a}t}\right) \quad (7)$$

where t is the duration of exposure (yr) and ϵ is the surface erosion rate (g cm^{-2} yr^{-1}). τ is a variable of integration.

^{21}Ne production by muons is taken from Heisinger et al. (2002a,b) and is:

$$N_{21,\mu-}(z) = f_{21}^*\int_0^t R_{\mu-}(z+\epsilon\tau)f_C f_d d\tau \quad (8)$$

$$N_{21,\mu f}(z) = \sigma_{0,21}\int_0^t \beta(z+\epsilon\tau)\Phi(z+\epsilon\tau)\bar{E}^{\alpha}(z+\epsilon\tau)N_i d\tau \quad (9)$$

These two expressions are composed of (i) a muon flux (for fast muon interactions) or stopping rate (for negative muon capture) integrated throughout the exposure history of the sample, multiplied by (ii) a likelihood or cross-section for production of ^{21}Ne. The integral terms are fully defined at any depth z by formulae given in Heisinger et al. (2002a,b) (see the Heisinger papers for the definition of the symbols). We evaluate them using the "Model 1A" MATLAB code of Balco (2017), setting the parameter α to 1 (see discussion in Borchers et al., 2016; Balco, 2017). Given exposure time t and erosion rate ϵ, this leaves as remaining unknown parameters a negative muon capture probability for ^{21}Ne production from Si (f_{21}^*; dimensionless), and a fast muon interaction cross-section for ^{21}Ne production from Si by 1 GeV muons ($\sigma_{0,21}$; barns). Although Heisinger et al. experimentally determined values for these parameters for reactions producing many cosmogenic nuclides, they did not do so for ^{21}Ne. Fernandez-Mosquera et al. (2008) estimated values from analogue reactions, but one of our aims in this paper is to independently constrain the value of these parameters from measured ^{21}Ne concentrations in the subsurface.

Thus, ^{21}Ne concentrations in our samples can be predicted with a forward model consisting of Equations 2, 3, 7, 8, and 9. Assuming the surface production rate of ^{21}Ne is known, this model has 8 unknown parameters: the exposure time t; surface erosion rate ϵ, neon closure age t_C; parameters describing the depth-dependence of spallogenic production Λ_{sp}, Λ_a, and f_a; and muon interaction parameters f_{21}^* and $\sigma_{0,21}$. It is not possible to estimate all these parameters at once; for example, many combinations of age and erosion rate can be made to fit the data well by adjusting the muon interaction cross-sections. In the case of radionuclides (e.g., ^{10}Be, ^{26}Al, ^{36}Cl, or ^{14}C) measured at a site that has experienced a long period of exposure at a low erosion rate, the situation can be simplified by assuming that the exposure time has been long enough that the nuclide concentrations at any depth have reached equilibrium between production, radioactive decay, and advection toward the surface due to erosion. In that case, given that the surface production rate is known, one can determine the erosion rate and the muon interaction cross-sections simultaneously (e.g., Stone et al., 1998; Balco, 2017). If the erosion rate is low enough in relation to the decay constant of the nuclide in question, then the muon interaction cross-sections can be determined independently of the erosion rate. However, that is not possible with ^{21}Ne, because, for a stable nuclide, as the erosion rate approaches zero, the time required for nuclide concentrations to reach production-erosion equilibrium approaches infinity. An additional complication (which is also applicable to radionuclides, although less important at low erosion rates), is that the erosion rate may have been unsteady, so that the effective erosion rate experienced during the time that the near-surface spallogenic ^{21}Ne inventory accumulated may be different from the effective erosion rate during the longer period of time in which the subsurface muon-produced ^{21}Ne inventory accumulated.

4.1. Zero-erosion end member

Because we cannot uniquely determine all unknown parameters, we will focus on obtaining limits on some of them. We begin by assuming that the surface erosion rate ϵ is zero and the surface ^{21}Ne production rate is 133 atoms g^{-1} yr^{-1}, which is computed by calculating the ^{10}Be production rate for the 'St' scaling method using version 3 of the online exposure age calculator described by Balco et al. (2008) and subsequently updated, and applying a total ^{21}Ne/^{10}Be production ratio of 4.0 (Balco and Shuster, 2009; Amidon et al., 2009; Kober et al., 2011). This leaves seven unknown parameters: t, t_C, Λ_{sp}, Λ_a, f_a, f_{21}^*, and $\sigma_{0,21}$. We fit this model to the data by minimizing a chi-squared misfit statistic:

$$M = \sum_j \left[\frac{N_{21,xs,p,j} - N_{21,xs,m,j}}{\sqrt{(\sigma N_{21,xs,p,j})^2 + (\sigma N_{21,xs,m,j})^2}} \right]^2 \quad (10)$$

where $N_{21,xs,m,j}$ and $\sigma N_{21,xs,m,j}$ are the measured excess ^{21}Ne concentration and measurement uncertainty for sample j, and $N_{21,xs,p,j}$ is the excess ^{21}Ne concentration predicted by the model for sample j. The uncertainty in the predicted concentration $\sigma N_{21,xs,p,j}$ stems from the uncertainty in estimating nucleogenic ^{21}Ne concentrations, which is in turn derived from uncertainties in measuring bulk U and Th concentrations. As discussed above, this uncertainty is likely much greater than the nominal uncertainty in the isotope dilution measurements. Assigning an expanded uncertainty to all

samples equally, however, would not change the relative weighting of samples in the model-fitting calculation, and we have little basis for arguing that any estimate of this expanded uncertainty would be accurate, so for fitting models to the data we assume $\sigma N_{21,xs,p,j} = 0$. The only constraint we imposed on the parameter values for this fitting exercise is that all must be greater than zero.

Figure 6 shows the result of fitting this model to the data. The minimum value of the fitting parameter M is 133 for 30 degrees of freedom (37 data less 7 fitted parameters). At face value this implies a vanishingly small probability that model-data misfit is consistent with measurement uncertainties, but this value for M is unrealistically high because we have not included any uncertainty in predicted ^{21}Ne concentrations stemming from uncertainty in U and Th concentrations, and also possibly because we did not include correlated uncertainties stemming from interlaboratory standardization. For example, if we assume a 25% uncertainty in estimates of nucleogenic ^{21}Ne (see discussion above), $M = 61$ for this model fit, so it is unclear how to best to evaluate the quality of the model fit. The best-fitting exposure age t is 4.1 Ma, in agreement with the apparent ^{10}Be exposure age, as expected from Figure 5. Optimal values of parameters related to spallogenic production are Λ_{sp} = 140.2 g cm^{-2}, which agrees precisely with values for ^{26}Al (144.7 ± 2.3) and ^{10}Be (140.5 ± 1.1) in the core determined by Borchers et al. (2016); Λ_a = 6.8 g cm−2; and f_a = 0.043.

The best-fitting neon closure age t_C is 156 Ma. This implies substantial nucleogenic ^{21}Ne concentrations in these samples, in the range 3-18 Matoms g^{-1} for etched samples and 7-19 Matoms g^{-1} for un-etched samples. Nucleogenic ^{21}Ne accounts for nearly all ^{21}Ne present in samples below ∼1000 g cm^{-2} depth (Fig. 6).

Because we assume a finite exposure time at zero erosion in this fitting exercise, best-fitting values for muon interaction cross-sections should provide upper limits on the true production rate due to muons. The best-fitting value for $\sigma_{0,21}$ is 0.0112 millibarns (mb). Fernandez-Mosquera et al. (2008) estimated this cross-section to be 0.79 mb for 190 GeV muon energy, based on analogue reactions whose cross-sections at 190 GeV were experimentally measured by Heisinger et al. (2002b). In our muon calculations, as discussed above, we assume that the energy dependence exponent α for this cross-section (see Heisinger et al., 2002b; Borchers et al., 2016) is 1, in which case the value of $\sigma_{0,21}$ implied by the estimate of Fernandez-Mosquera et al. (2008) is $0.79/(190^1) = 0.0042$ mb. This is consistent with the upper limit represented by our best-fitting value. On the other hand, our best-fitting value for the negative muon capture cross-section f_{21}^* is zero, implying that ^{21}Ne is not produced by negative muon capture. This agrees with the assessment of Kober et al. (2011), who proposed that no suitable negative muon capture reaction on Si exists. However, Fernandez-Mosquera et al. (2008) proposed several possible reactions. Our measurements are most consistent with the argument that ^{21}Ne production by this pathway is negligible.

4.2. Steady-erosion end member

We now attempt to fit the data under the opposite end member assumption that the site has experienced slow erosion for a much longer period of time than implied by the apparent surface exposure age. Independent geologic evidence indicates that the last significant topographic development in the Dry Valleys preceded 14.5 Ma (Sugden et al., 1999; Sugden and Denton, 2004; Lewis et al., 2006). Thus, we assume that t =

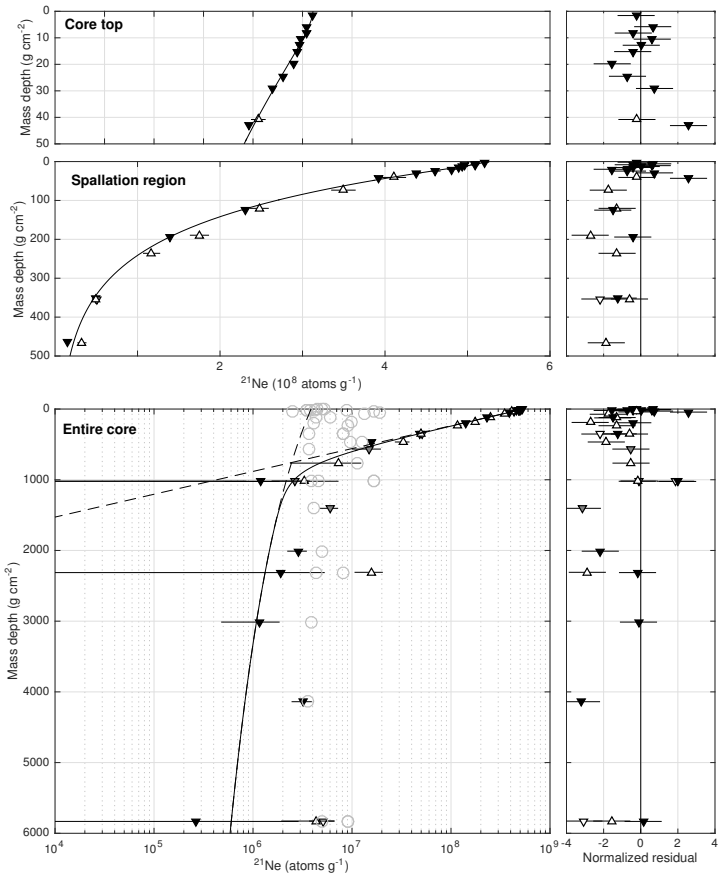

Figure 6: Fit of zero-erosion model to ^{21}Ne concentrations in the core. The left panels show data with the best-fitting model; the right panels show normalized residuals. The data are the same in all panels, but the y-axes are different so as to adequately show details in all parts of the core. Gray circles (in lower panel only) show nucleogenic ^{21}Ne concentrations predicted by best-fitting model parameters for each sample, and black symbols (with same symbology as in Figure 2) show corresponding cosmogenic ^{21}Ne concentrations (thus, these are different from the data plotted in Figure 2, which are total excess ^{21}Ne concentrations). The solid line shows cosmogenic ^{21}Ne concentrations predicted by the best-fitting parameters, and the dashed lines in the lower panel show predictions for spallogenic and muon-produced ^{21}Ne.

14.5 Ma. In addition, we simplify the optimization problem by also assuming Λ_{sp} = 140 g cm^{-2}. This leaves ϵ, Λ_a, f_a, t_C, $\sigma_{0,21}$, and f_{21}^* as unknown parameters. Again, here we impose only the constraint that all parameters must be positive.

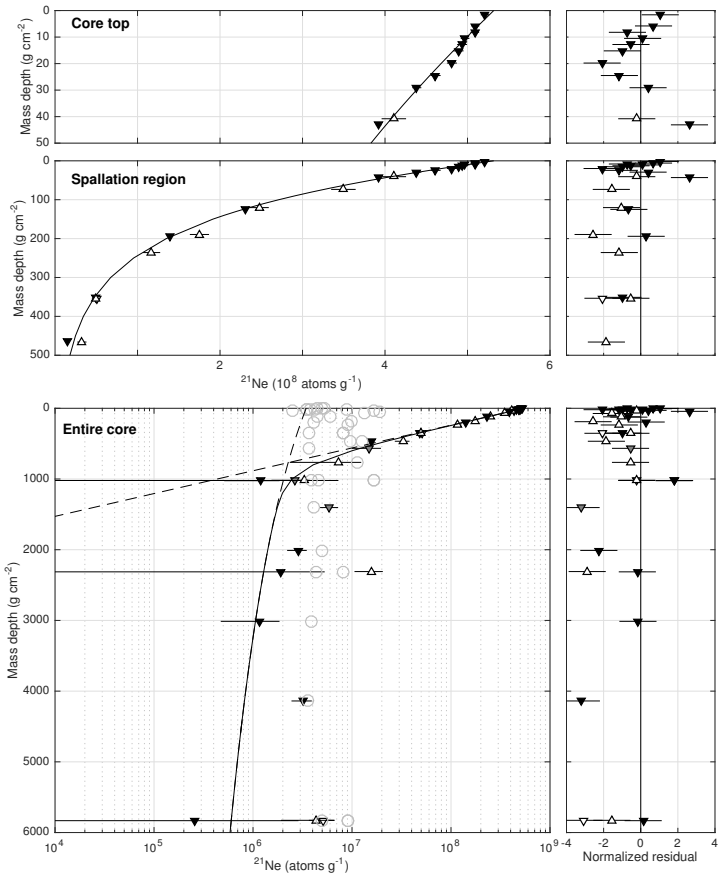

Figure 7: Fit of 14.5 Ma steady-erosion model to ^{21}Ne concentrations in the core. Figure elements are the same as in Figure 6.

Figure 7 shows the result of fitting this model to the data. The minimum value of the fitting parameter M is the same, and the overall fit to the data is similar, as is evident by comparison of Figures 6 and 7. The best-fitting erosion rate over 14.5 Ma is 3.3×10^{-5} g cm^{-2} yr^{-1}, or 0.14 m Myr^{-1} for the mean rock density in the core of 2.31 g cm^{-3}. The best-fitting value for t_C is again 156 Ma; as we expect from the fact that U and Th concentrations are not correlated with depth in the core, this value is not sensitive to assumptions about the exposure history.

Assuming steady erosion for a long period of time makes it difficult to fit the near-surface spallogenic ^{21}Ne profile; this scenario requires Λ_a = 36 g cm^{-2} and f_a = 0.15, which are probably too large to be realistic (e.g., Masarik and Reedy, 1995; Argento

et al., 2013), and even with these much larger values the fit to the data is poor near the surface (Fig 7). Heuristically, this is not surprising, because erosion acts to replace the nuclide inventory produced at the surface with that produced in the subsurface region that is not affected by albedo effects. Thus, in the presence of erosion, a more extreme reduction in the production rate at the surface is needed to yield an observable effect in the near-surface concentrations. The difficulty of fitting the near-surface profile with a steady-erosion model would tend to suggest that the true exposure history of the site is transient and involves relatively rapid removal of meter-scale layers of rock, with near-zero erosion between stripping events. This is potentially consistent with the stratified nature of the bedrock: erosion at this site could occur primarily by lateral backwearing of successive strata rather than steady surface degradation.

Again, the best-fitting value for f_{21}^* is zero, implying no production of ^{21}Ne by negative muon capture. The best fitting value of the fast muon interaction cross-section $\sigma_{0,21}$ for this scenario is 0.0033 mb. Given the assumption that the total exposure history of the site can span no more than 14.5 Ma, this should provide a minimum constraint on the muon production rate, so again this is consistent with the estimate from analogue reactions by Fernandez-Mosquera et al. (2008).

4.3. Uncertainty analysis

The fact that models with very different exposure histories can be equivalently fit to the data indicates that an attempt to estimate a formal uncertainty in any of our parameter estimates for a particular one of these models would not be meaningful. However, one important conclusion of the discussion above is that our measurements imply that production of ^{21}Ne by negative muon capture is zero or at least negligible. Thus, in this section we explore further whether nonzero negative muon capture production would be consistent with the observations, or if it is entirely precluded. In addition, we investigate the uncertainty in the estimate of Ne closure age. To do this, we use a simplified model in which we assume values for the muon production parameters f_{21}^* and $\sigma_{0,21}$, and simplify Equation 7 as:

$$N_{21,sp}(z) = N_{21,sp}(0)e^{\frac{z}{\Lambda_{sp}}} \tag{11}$$

The effect of this is that the spallogenic ^{21}Ne inventory is parameterized simply by a surface nuclide concentration $N_{21,sp}(0)$ instead of the exposure age and erosion rate, which accommodates transient exposure histories by permitting spallogenic and muon-produced inventories to reflect different effective erosion rates. In other words, it permits the muon-produced inventory to have accumulated over a longer time than the spallogenic inventory, which would take place, for example, in the scenario of unsteady erosion by backwearing of successive strata suggested above. We also disregard measurements in the upper 20 g cm^{-2} of the core so that it is not necessary to fit the near-surface deviation from a single exponential profile. We then assume Λ_{sp} = 140 g cm^{-2} and a total exposure time of 14.5 Ma as above. This leaves only the neon closure age t_C, the erosion rate ϵ, and the spallogenic surface nuclide concentration $N_{21,sp}(0)$ as fitting parameters. Finally, we constrain all parameters to be greater than zero, and for computational efficiency constrain the erosion rate to be less than 0.2 m Myr^{-1},

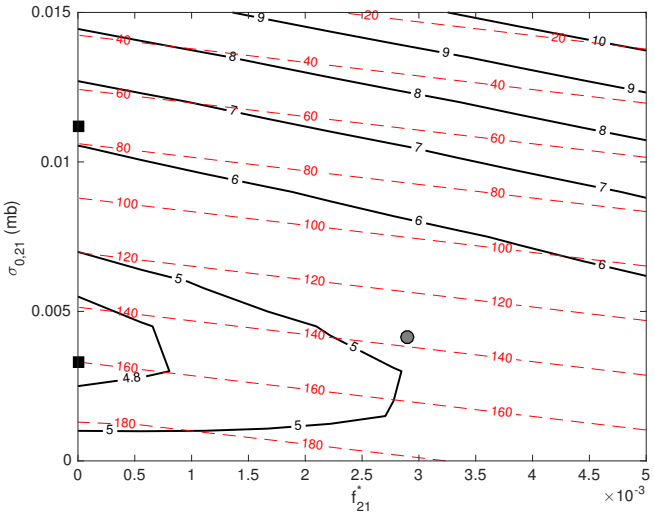

Figure 8: The solid black lines are contours of best attainable value of the reduced chi-squared misfit statistic χ^2/ν (e.g., M as defined above divided by the number of degrees of freedom) for a range of specified values of f^*_{21} and $\sigma_{0,21}$, using the simplified 14.5 Ma steady erosion model and the constraints described in the text. Note that values of the fit statistic shown here are not comparable to those discussed for the complete models in the previous section, because near-surface data have been excluded and the fitting parameters are different. In addition, they are calculated assuming zero uncertainty in predicted nucleogenic ^{21}Ne concentrations (see text). Thus, they should not be taken to imply a realistic probability-of-fit. The gray circle shows the values for muon interaction cross-sections proposed by Fernandez-Mosquera et al. (2008), and the black squares show best-fitting values for the simple-exposure and steady-erosion models described in the previous sections, which represent maximum and minimum constraints on f^*_{21}, respectively. The dashed red lines are contours of the neon closure age (in Ma) in the best-fitting model for each (f^*_{21}, $\sigma_{0,21}$) pair.

which is slightly higher than the maximum erosion rate permitted by the surface ^{21}Ne concentration.

Figure 8 shows the results of this fitting exercise for a range of values of f_{21}^{*} and $\sigma_{0,21}$. Although zero negative muon capture production results in the best fit, the observations can be fit nearly as well with some negative muon capture, as long as total muon production remains relatively low. This is because nearly all the observed excess ^{21}Ne in deep samples is nucleogenic rather than muon-produced, which results in poor resolution on muon production rates overall. Another important point highlighted in Figure 8 is that prescribing higher values of f_{21}^{*} and $\sigma_{0,21}$ in this calculation, without permitting higher erosion rates than allowed by the surface ^{21}Ne concentration, apportions more of the excess ^{21}Ne concentration in the deep part of the core to cosmogenic rather than nucleogenic production, which decreases the best-fitting neon closure age. The approximate correspondence between the closure temperature of Ne in quartz (Shuster and Farley, 2005) and that of the apatite fission-track system implies that the true neon closure age of these samples must be greater than AFT ages of ~150 Ma at lower elevations nearby in the Dry Valleys (Gleadow and Fitzgerald, 1987, P. Fitzgerald, written communication), and in addition it must presumably be lower than the 183 Ma emplacement age of the Ferrar dolerite, sills of which intrude the Beacon Fm. close to the core site (Burgess et al., 2015). This criterion also favors lower values for muon production rates, although, again, it does not completely preclude some contribution from negative muon capture production. As discussed above, best-fitting models have a neon closure age near 160 Ma, but the data can be fit nearly as well with values between ~130-180 Ma. This is effectively indistinguishable from closure ages between 133-351 Ma obtained from the Mackay Glacier erratics discussed above.

5. Discussion and conclusions

In this section we highlight potentially useful conclusions of this study related to (i) nucleogenic ^{21}Ne systematics in Beacon Group sandstone, and (ii) production of cosmogenic ^{21}Ne in quartz by muon interactions.

5.1. Nucleogenic ^{21}Ne and the (U-Th)/Ne age of Beacon Group sandstone in the Dry Valleys area

Quartz in Beacon Group sandstones contains significant concentrations of nucleogenic ^{21}Ne. The mean and standard deviation of nucleogenic ^{21}Ne concentrations in etched core samples implied by the best-fitting neon closure age of ~156 Ma is 5.2 ± 3.4 Matoms g^{-1}, which is effectively the same as 7.1 ± 2.0 Matoms g^{-1} in etched quartz measured in Mackay Glacier erratics. For un-etched core samples, it is 11.1 ± 3.6 Matoms g^{-1}. Middleton et al. (2012) also estimated nucleogenic ^{21}Ne concentrations in a set of Beacon Group sandstones from a different location in the Dry Valleys by inferring nucleogenic ^{21}Ne from measurements of fissiogenic ^{129}Xe concentrations and the assumption of simultaneous Ne and Xe closure. Their samples were HF-etched, but not as extensively as ours (a single 24-hour period at room temperature), and they inferred an average nucleogenic ^{21}Ne concentration of 7.7 ± 2.4 Matoms g^{-1}, which is consistent with our results. They did not measure U and Th concentrations. Thus, these

studies are consistent and, in addition, the observation that the best-fitting (U-Th)/Ne closure age is effectively indistinguishable from Ferrar emplacement tends to support the assumption of simultaneous Ne and Xe closure (which would be expected in the case of rapid cooling after a reheating event at shallow depth, but not in the case of prolonged cooling due to slow exhumation).

The results of both studies are potentially useful for surface exposure dating using ^{21}Ne in this lithology, because they show that it is possible to estimate nucleogenic ^{21}Ne concentrations independently of the Ne measurements themselves either by (i) Xe measurements and the assumption of simultaneous Ne and Xe closure, or (ii) U and Th measurements and an assumed closure age. Potentially, this could significantly improve the precision of cosmogenic ^{21}Ne measurements and facilitate exposure-dating of relatively young surfaces. However, both studies also show that nucleogenic ^{21}Ne concentrations are quite variable among different samples of quartz from Beacon Group sandstones, and we find that they are strongly affected by sample pretreatment and etching. In addition, replicate measurements of U and Th on individual quartz samples show substantial excess scatter. These observations indicate that estimates of nucleogenic ^{21}Ne based on U/Th concentrations and an assumed closure age most likely have precision no better than ~20%, and possibly much worse. If mean nucleogenic ^{21}Ne in Beacon Group sandstone quartz is 7 Matoms g^{-1}, this implies an uncertainty in estimating nucleogenic ^{21}Ne and thus also in estimating cosmogenic ^{21}Ne of at least 1.5 Matoms g−1, which is equivalent to an uncertainty in exposure age of ca. 75,000 years at sea level or ca. 40,000 years at 1 km elevation. Thus, nucleogenic ^{21}Ne estimates for this lithology are not accurate enough for ^{21}Ne exposure-dating of, for example, Last-Glacial-Maximum-age deposits in the age range 15,000-25,000 years, but are likely accurate enough for useful exposure-age measurements on deposits dating to previous glacial maxima (> 0.15 Ma). The precision of nucleogenic ^{21}Ne estimates could most likely be improved by investigating the causes of scatter in U and Th concentrations.

5.2. Cosmogenic ^{21}Ne production by muons

We cannot precisely estimate muon interaction cross-sections from our subsurface ^{21}Ne concentrations, mainly because at depths below ca. 1000 g cm^{-2} where cosmogenic ^{21}Ne is expected to be dominantly muon-produced, most ^{21}Ne is nucleogenic and muon produced ^{21}Ne represents only a small fraction of the total. In addition, steady-state assumptions that can be used for this purpose for radionuclides are not applicable for stable nuclides. However, the model-fitting exercises above place some bounds on these values. First, our measurements are most consistent with negligible ^{21}Ne production by negative muon capture. As far as we are aware, there is no other observational evidence for measurable ^{21}Ne production by this mechanism that would contradict this. Theoretical discussions of this production mechanism disagree: Kober et al. (2011) argued that no likely negative muon capture reactions exist, and in addition Lal (1988) did not propose any such reactions, but on the other hand Fernandez-Mosquera et al. (2008) proposed possible reactions. Although our observations are not conclusive, they suggest that, in fact, negative muon capture production is negligible. However, our observations are consistent with measurable ^{21}Ne production by fast muon interactions. Limits on the fast muon interaction cross-section derived from end-member model fitting exercises are consistent with the proposed cross-section inferred from analogue

measurements by Fernandez-Mosquera et al. (2008) as well as the reasoning of Kober et al. (2011) that fast muon production of ^{21}Ne should be less than 2% of total surface production. Thus, we propose that available evidence indicates that the most sensible approach to computing ^{21}Ne production rates due to muon interactions is to (i) assume zero negative muon capture production, and (ii) adopt the fast muon interaction cross-section estimate of Fernandez-Mosquera et al. (2008). This approach implies that ^{21}Ne production by muons is 0.2 atoms g^{-1} yr^{-1} (~1% of total surface production) at sea level.

5.3. Effect on existing production rate estimates for ^{21}Ne

Balco and Shuster (2009) estimated the ^{21}Ne/^{10}Be production ratio to be 4.08 using a set of ^{21}Ne measurements on samples of Beacon Group sandstone from the Dry Valleys. This estimate (i) assumed that zero nucleogenic ^{21}Ne was present, and (ii) inferred a total production rate due to muons of 0.66 atoms g^{-1} yr^{-1} at sea level. Our results here indicate that both (i) and (ii) are incorrect. Thus, we revised the calculations in that paper to assume that (i) nucleogenic ^{21}Ne in those samples is present at the average concentration estimated here for core samples, and (ii) muon production of ^{21}Ne is as suggested above. These adjustments result in a 5% increase in the estimated ^{21}Ne/^{10}Be production ratio, to 4.27. However, the measurements in Balco and Shuster (2009) were collected on the BGC MAP-II system prior to the intercomparison exercise of Vermeesch et al. (2015), and renormalizing these data to reference values for the CRONUS-A and CREU-1 standards has the opposite effect, resulting in a revised estimate of 4.03 that is effectively the same as the originally published value.

6. Data and code availability

MATLAB scripts used for model fitting and production of figures, as well as all tables and supplementary data in spreadsheet form, are available for purposes of review of this paper at the following URL:

`http://hess.ess.washington.edu/repository/BCO_neon_201806`

7. Acknowledgements.

Analytical work at BGC was supported primarily by the Ann and Gordon Getty Foundation and in part by U.S. National Science Foundation grant EAR-0345949. We thank Kevin Norton and Richard Jones for supplying aliquots of quartz from the Mackay Glacier erratics described in Jones et al. (2015), Brent Goehring for preparing Tulane-sourced samples, Lindsey Hedges and Ken Farley for U/Th measurements at Caltech, and Tim Becker for assistance with mass-spectrometric measurements.

Tables

748

Table 1. Excess ^{21}Ne with respect to atmosphere, U, and Th concentrations for Beacon Heights core samples. ^{21}Ne concentrations from different labs have been normalized to a common value of the CREU-1 and CRONUS-A interlaboratory comparison standards. See text and supplementary material for details.

Depth (cm)	Midpoint mass depth (g cm^{-2})	Excess ^{21}Ne (Matoms g^{-1})	No. of analyses	[U] (ppm)	[Th] (ppm)	Sample prep-aration at:	System for Ne analysis	U/Th analysis at:
0-1.4	1.6	525.6 +/- 5.1	3	0.085	0.356	UW	BGC-MAPII	BGC
2-3	5.8	514.4 +/- 4.8	4	0.077	0.437	UW	BGC-MAPII	BGC
3-4	8.2	514.0 +/- 5.3	3	0.109	0.385	UW	BGC-MAPII	BGC
4-5	10.5	500.5 +/- 5.3	3	0.087	0.258	UW	BGC-MAPII	BGC
5-6	12.8	502.3 +/- 5.9	2	0.276	0.453	UW	BGC-MAPII	BGC
6-7	15.2	493.2 +/- 6.3	2	0.073	0.336	UW	BGC-MAPII	BGC
8-9	19.8	484.5 +/- 6.0	2	0.070	0.266	UW	BGC-MAPII	BGC
10-11	24.5	465.1 +/- 6.1	2	0.069	0.262	UW	BGC-MAPII	BGC
12-13	29.1	441.0 +/- 5.5	2	0.041	0.196	UW	BGC-MAPII	BGC
17-18	40.8	427 +/- 15	1	0.726	1.279	CRPG	CRPG	CRPG
18-19	43.1	411.3 +/- 3.4	4	0.258	1.468	UW	BGC-MAPII	BGC
31-32	73.5	363 +/- 15	1	0.459	1.332	CRPG	CRPG	CRPG
51-52	120.3	253.5 +/- 12	1	0.240	0.522	CRPG	CRPG	CRPG
53-54	124.9	234.4 +/- 3.2	2	0.088	0.356	UW	BGC-MAPII	BGC
81-82	189.4	185 +/- 12	1	0.389	0.846	CRPG	CRPG	CRPG
83-84	194.1	143.9 +/- 2.4	2	0.064	0.276	UW	BGC-MAPII	BGC
101-102	235.9	126 +/- 10	1	0.336	0.859	CRPG	CRPG	CRPG
151-152	351.1	52.6 +/- 1.5	2	0.070	0.219	UW	BGC-MAPII	BGC
152-153	353.4	59.5 +/- 2.2	2	0.334	1.005	CRPG	BGC-MAPII	BGC
152-153	353.4	57.6 +/- 4.8	1	0.334	1.005	CRPG	CRPG	CRPG
201-202	463.8	25.1 +/- 1.1	2	0.110	0.369	UW	BGC-MAPII	BGC
202-203	466.0	45.3 +/- 5.5	1	0.529	1.034	CRPG	CRPG	CRPG
247-248	566.2	18.5 +/- 4.8	2	0.080	0.272	Tulane	BGC-Ohio	BGC
335-336	764.8	18.8 +/- 5.0	1	0.464	0.966	CRPG	CRPG	CRPG
447-448	1018	6.5 +/- 1.1	2	0.091	0.268	Tulane	BGC-Ohio	BGC
448-449	1021	15.7 +/- 1.9	1	0.348	2.375	CRPG	BGC-MAPII	BGC
448-449	1021	20.1 +/- 4.0	1	0.348	2.375	CRPG	CRPG	CRPG
449-451	1024	5.72 +/- 0.67	2	0.076	0.246	UW	BGC-MAPII	BGC
613-615	1404	10.0 +/- 1.3	2	0.104	0.260	Tulane	BGC-Ohio	BGC
860-862	2010	7.86 +/- 0.64	2	0.122	0.302	UW	BGC-MAPII	BGC
996-998	2309	23.8 +/- 4.9	1	0.272	0.871	CRPG	CRPG	CRPG
998-1000	2313	6.2 +/- 3.4	2	0.062	0.267	UW	BGC-MAPII	BGC
1300-1302	3013	5.00 +/- 0.69	2	0.054	0.157	UW	BGC-MAPII	BGC
1784-1786	4139	6.81 +/- 0.74	2	0.095	0.254	UW	BGC-MAPII	BGC
2518-2520	5827	14.2 +/- 1.5	1	0.369	1.038	CRPG	BGC-MAPII	BGC
2518-2520	5827	13.3 +/- 2.4	1	0.369	1.038	CRPG	CRPG	CRPG
2520-2522	5832	5.2 +/- 2.6	2	0.082	0.263	UW	BGC-MAPII	BGC

749

750

Table 2. Excess ^{21}Ne, U, and Th concentrations for sandstone erratics at Mackay Glacier collected by Jones et al. (2015). Sample information and ^{10}Be concentrations are documented in that reference. Uncertainty estimates for closure ages assume 25% uncertainty in total alpha particle production; see text for details.

Sample name	Excess ^{21}Ne (Matoms g^{-1})	No. of Ne analyses	[U] (ppm)	[Th] (ppm)	[^{10}Be] (atoms g^{-1})	Calculated cosmogenic ^{21}Ne (Matoms g^{-1})	Calculated nucleogenic ^{21}Ne (Matoms g^{-1})	^{21}Ne closure age (Ma)
GR47	8.0 +/- 1.3	3	0.085	0.344	88730 +/- 22700	0.362 +/- 0.093	7.6 +/- 1.3	273 +/- 83
GR48	3.0 +/- 1.0	2	0.051	0.201	73410 +/- 3100	0.300 +/- 0.013	2.7 +/- 1.0	165 +/- 74
GR51	6.5 +/- 1.8	2	0.100	0.286	209700 +/- 34900	0.856 +/- 0.142	5.6 +/- 1.8	208 +/- 84
GR52	11.2 +/- 1.8	2	0.139	0.205	263200 +/- 9220	1.074 +/- 0.038	10.1 +/- 1.8	351 +/- 108
GR53B	8.1 +/- 1.2	2	0.115	0.238	73850 +/- 3040	0.301 +/- 0.012	7.8 +/- 1.2	291 +/- 85
GR54	9.5 +/- 1.6	2	0.175	0.198	87690 +/- 23100	0.358 +/- 0.094	9.2 +/- 1.6	276 +/- 84
GR56	7.32 +/- 0.79	6	0.210	0.505	69500 +/- 3910	0.284 +/- 0.016	7.04 +/- 0.79	135 +/- 37
GR59	8.2 +/- 1.0	4	0.137	0.345	63260 +/- 2550	0.258 +/- 0.010	7.9 +/- 1.0	227 +/- 64
GR62B	6.1 +/- 1.4	2	0.094	0.221	64770 +/- 17100	0.264 +/- 0.070	5.8 +/- 1.5	252 +/- 90
GR64	8.2 +/- 1.0	5	0.184	0.458	30920 +/- 10200	0.126 +/- 0.042	8.1 +/- 1.0	175 +/- 49
GR67	4.7 +/- 1.1	2	0.100	0.186	38650 +/- 6890	0.158 +/- 0.028	4.5 +/- 1.1	202 +/- 71
CC90	8.9 +/- 1.0	3	0.153	0.201	6249 +/- 853	0.025 +/- 0.003	8.9 +/- 1.0	293 +/- 80
CC95	7.0 +/- 1.1	3	0.162	0.330	44990 +/- 2180	0.184 +/- 0.009	6.8 +/- 1.1	182 +/- 54

References

Amidon, W. H., Rood, D. H., Farley, K. A., 2009. Cosmogenic ^{3}He and ^{21}Ne production rates calibrated against ^{10}Be in minerals from the Coso volcanic field. Earth and Planetary Science Letters 280 (1), 194–204.

Argento, D. C., Reedy, R. C., Stone, J. O., 2013. Modeling the Earth's cosmic radiation. Nuclear Instruments and Methods in Physics Research Section B: Beam Interactions with Materials and Atoms 294, 464–469.

Balco, G., 2017. Production rate calculations for cosmic-ray-muon-produced ^{10}Be and ^{26}Al benchmarked against geological calibration data. Quaternary Geochronology.

Balco, G., Shuster, D. L., 2009. Production rate of cosmogenic ^{21}Ne in quartz estimated from ^{10}Be, ^{26}Al, and ^{21}Ne concentrations in slowly eroding antarctic bedrock surfaces. Earth and Planetary Science Letters 281 (1), 48–58.

Balco, G., Stone, J., Lifton, N., Dunai, T., 2008. A complete and easily accessible means of calculating surface exposure ages or erosion rates from ^{10}Be and ^{26}Al measurements. Quaternary Geochronology 3, 174–195.

Balco, G., Stone, J. O., Sliwinski, M. G., Todd, C., 2014. Features of the glacial history of the Transantarctic Mountains inferred from cosmogenic ^{26}Al, ^{10}Be and ^{21}Ne concentrations in bedrock surfaces. Antarctic Science 26 (06), 708–723.

Bernet, M., Gaupp, R., 2005. Diagenetic history of triassic sandstone from the beacon supergroup in central victoria land, antarctica. New Zealand Journal of Geology and Geophysics 48 (3), 447–458.
URL `https://doi.org/10.1080/00288306.2005.9515125`

Borchers, B., Marrero, S., Balco, G., Caffee, M., Goehring, B., Lifton, N., Nishiizumi, K., Phillips, F., Schaefer, J., Stone, J., 2016. Geological calibration of spallation production rates in the CRONUS-Earth project. Quaternary Geochronology 31, 188–198.

Burgess, S., Bowring, S., Fleming, T., Elliot, D., 2015. High-precision geochronology links the Ferrar large igneous province with early-Jurassic ocean anoxia and biotic crisis. Earth and Planetary Science Letters 415, 90–99.

Cox, S. E., Farley, K. A., Cherniak, D. J., 2015. Direct measurement of neon production rates by (α, n) reactions in minerals. Geochimica et Cosmochimica Acta 148, 130–144.

Dunai, T., 2010. Cosmogenic Nuclides: Principles, Concepts, and Applications in the Earth Surface Sciences. Cambridge University Press: Cambridge, UK.

Farley, K., Wolf, R., Silver, L., 1996. The effects of long alpha-stopping distances on (U-Th)/He ages. Geochimica et Cosmochimica Acta 60 (21), 4223–4229.

Fernandez-Mosquera, D., Marti, H., Hahm, D., Vidal-Romani, J., Braucher, R., Bourlès, D., 2008. Muon produced neon in quartz at large depths: BeNe project progress report. Geochimica Et Cosmochimica Acta 72 (12), A265.

Gleadow, A., Fitzgerald, P., 1987. Uplift history and structure of the Transantarctic Mountains: new evidence from fission track dating of basement apatites in the Dry Valleys area, southern Victoria Land. Earth and Planetary Science Letters 82 (1-2), 1–14.

Heisinger, B., Lal, D., Jull, A. J. T., Kubik, P., Ivy-Ochs, S., Knie, K., Nolte, E., 2002a. Production of selected cosmogenic radionuclides by muons: 2. Capture of negative muons. Earth and Planetary Science Letters 200 (3-4), 357–369.

Heisinger, B., Lal, D., Jull, A. J. T., Kubik, P., Ivy-Ochs, S., Neumaier, S., Knie, K., Lazarev, V., Nolte, E., 2002b. Production of selected cosmogenic radionuclides by muons 1. Fast muons. Earth and Planetary Science Letters 200 (3-4), 345–355.

Hetzel, R., Niedermann, S., Ivy-Ochs, S., Kubik, P. W., Tao, M., Gao, B., 2002. ^{21}Ne versus ^{10}Be and ^{26}Al exposure ages of fluvial terraces: the influence of crustal Ne in quartz. Earth and Planetary Science Letters 201 (3), 575–591.

House, M., Farley, K., Stockli, D., 2000. Helium chronometry of apatite and titanite using nd-yag laser heating. Earth and Planetary Science Letters 183 (3-4), 365–368.

Jones, R., 2015. Late Cenozoic Behaviour of two Transantarctic Mountains Outlet Glaciers. Ph.D. thesis, Victoria University of Wellington.

Jones, R., Mackintosh, A., Norton, K. P., Golledge, N. R., Fogwill, C., Kubik, P. W., Christl, M., Greenwood, S. L., 2015. Rapid Holocene thinning of an East Antarctic outlet glacier driven by marine ice sheet instability. Nature Communications 6, 8910.

Jull, A. T., Scott, E. M., Bierman, P., 2015. The CRONUS-Earth inter-comparison for cosmogenic isotope analysis. Quaternary Geochronology 26, 3–10.

Kober, F., Alfimov, V., Ivy-Ochs, S., Kubik, P., Wieler, R., 2011. The cosmogenic ^{21}Ne production rate in quartz evaluated on a large set of existing ^{21}Ne–^{10}Be data. Earth and Planetary Science Letters 302 (1), 163–171.

Kober, F., Ivy-Ochs, S., Kubik, P., Wieler, R., 2008. Comparison of age pairs derived from cosmogenic ^{21}Ne and ^{10}Be. Geochimica Et Cosmochimica Acta 72, A485.

Lal, D., 1988. In situ produced cosmogenic isotopes in terrestrial rocks. Ann. Rev. Earth Planet. Sci. 16, 355–388.

Lewis, A., Marchant, D., Ashworth, A., Hemming, S., Machlus, M., 2007. Major middle Miocene global climate change: evidence from East Antarctica and the Transantarctic Mountains. Geological Society of America Bulletin 119, 1449–1461.

Lewis, A., Marchant, D., Kowalewski, D., Baldwin, S., Webb, L., 2006. The age and origin of the Labyrinth, western Dry Valleys, Antarctica: evidence for extensive middle Miocene subglacial floods and freshwater discharge to the Southern Ocean. Geology 34, 513–516.

Lifton, N., Sato, T., Dunai, T. J., 2014. Scaling in situ cosmogenic nuclide production rates using analytical approximations to atmospheric cosmic-ray fluxes. Earth and Planetary Science Letters 386, 149–160.

Masarik, J., Reedy, R. C., 1995. Terrestrial cosmogenic-nuclide production systematics calculated from numerical simulations. Earth and Planetary Science Letters 136 (3-4), 381–395.

Masarik, J., Wieler, R., 2003. Production rates of cosmogenic nuclides in boulders. Earth and Planetary Science Letters 216, 201–208.

McElroy, C., Rose, G., 1987. Geology of the beacon heights area, southern victoria land. Antarctica: New Zealand Geological Survey Miscellaneous Series Map 15.

Middleton, J. L., Ackert, R. P., Mukhopadhyay, S., 2012. Pothole and channel system formation in the McMurdo Dry Valleys of Antarctica: new insights from cosmogenic nuclides. Earth and Planetary Science Letters 355, 341–350.

Niedermann, S., 2002. Cosmic-ray-produced noble gases in terrestrial rocks: dating tools for surface processes. In: Porcelli, D., Ballentine, C., Wieler, R. (Eds.), Noble gases in geochemistry and cosmochemistry. Vol. 47 of Reviews in Mineralogy and Geochemistry. Mineralogical Society of America, pp. 731–784.

Niedermann, S., Graf, T., Marti, K., 1993. Mass spectrometric identification of cosmic-ray-produced neon in terrestrial rocks with multiple neon components. Earth and Planetary Science Letters 118 (1-4), 65–73.

Phillips, F. M., Argento, D. C., Balco, G., Caffee, M. W., Clem, J., Dunai, T. J., Finkel, R., Goehring, B., Gosse, J. C., Hudson, A. M., et al., 2016. The CRONUS-Earth project: a synthesis. Quaternary Geochronology 31, 119–154.

Phillips, F. M., Stone, W. D., Fabryka-Martin, J. T., 2001. An improved approach to calculating low-energy cosmic-ray neutron fluxes near the land/atmosphere interface. Chemical Geology 175 (3), 689–701.

Shuster, D. L., Farley, K. A., 2005. Diffusion kinetics of proton-induced ^{21}Ne, ^{3}He, and ^{4}He in quartz. Geochimica et Cosmochimica Acta 69 (9), 2349–2359.

Stone, J., Evans, J., Fifield, L., Allan, G., Cresswell, R., 1998. Cosmogenic chlorine-36 production in calcite by muons. Geochimica et Cosmochimica Acta 62 (3), 433–454.

Stone, J. O., 2000. Air pressure and cosmogenic isotope production. Journal of Geophysical Research 105 (B10), 23753–23759.

Sugden, D., Denton, G., 2004. Cenozoic landscape evolution of the Convoy Range to Mackay Glacier area, Transantarctic Mountains: onshore to offshore synthesis. Geological Society of America Bulletin 116, 840–857.

Sugden, D., Summerfield, M., Denton, G., Wilch, T., McIntosh, W., Marchant, D., Rutford, R., 1999. Landscape development in the Royal Society Range, southern Victoria Land, Antarctica: stability since the mid-Miocene. Geomorphology 28, 181–200.

Summerfield, M., Stuart, F., Cockburn, H., Sugden, D., Denton, G., Dunai, T., Marchant, D., 1999. Long-term rates of denudation in the Dry Valleys, Transantarctic Mountains, southern Victoria Land, Antarctica based on in-situ-produced cosmogenic ^{21}Ne. Geomorphology 27 (1), 113–129.

Vermeesch, P., Balco, G., Blard, P.-H., Dunai, T. J., Kober, F., Niedermann, S., Shuster, D. L., Strasky, S., Stuart, F. M., Wieler, R., et al., 2015. Interlaboratory comparison of cosmogenic ^{21}Ne in quartz. Quaternary Geochronology 26, 20–28.

Zimmermann, L., Blard, P. H., Burnard, P., Medynski, S., Pik, R., Puchol, N., 2012. A new single vacuum furnace design for cosmogenic ^{3}He dating. Geostandards and Geoanalytical Research 36 (2), 121–129.

Supplementary Figure SF1. Ne isotope ratios measured in all heating steps for all core samples. Ellipses are 68% confidence regions. The black dot is the isotope composition of atmospheric Ne and the black lines show the atmospheric-cosmogenic mixing line (Niedermann, 2000; the separation of the lines reflects the uncertainty in the isotope composition of cosmogenic Ne). The color-coding reflects extraction temperature: light blue, <500°C; light purple, 500-1000°; light red, 1000°. The data in the two panels are the same; only the axis limits differ. Note that although some of the uncertainty ellipses do not overlap the cosmogenic-atmospheric mixing line, the ellipses are supposed to be 68% uncertainty regions. Thus, if they are drawn correctly and the true isotope compositions of all heating steps do, in fact, line on the mixing line, then we expect 32% of the ellipses, or 62 of 185 ellipses shown here, to fail to overlap with the mixing line. In fact, only 23 ellipses do not overlap with the mixing line, which suggests that variance of isotope ratios around the mixing line is due to measurement error alone and also that measurement uncertainties may have been slightly overestimated.

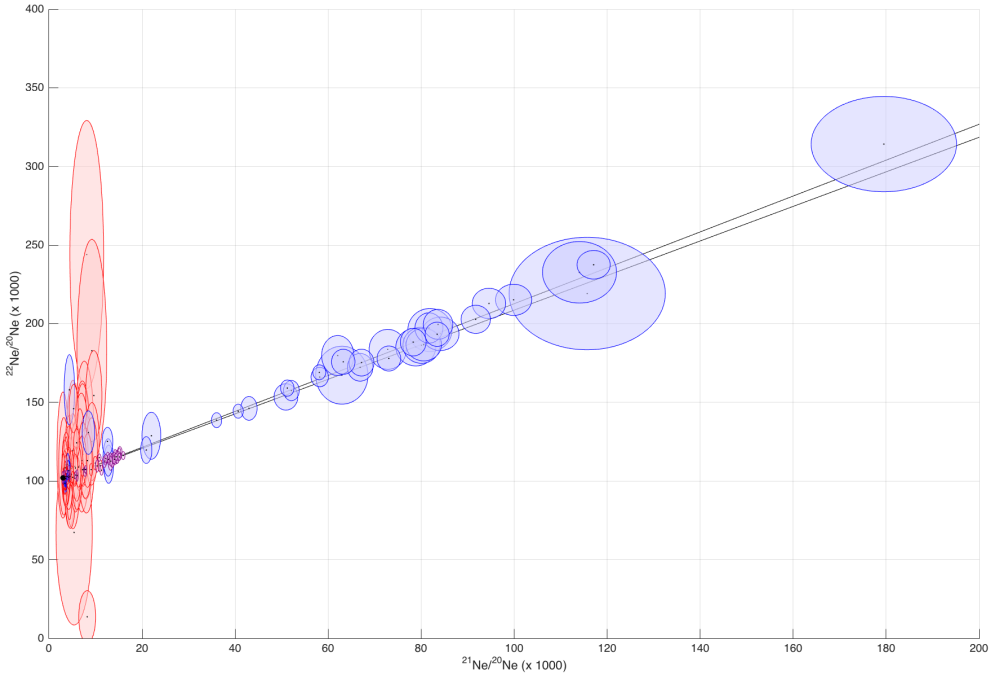

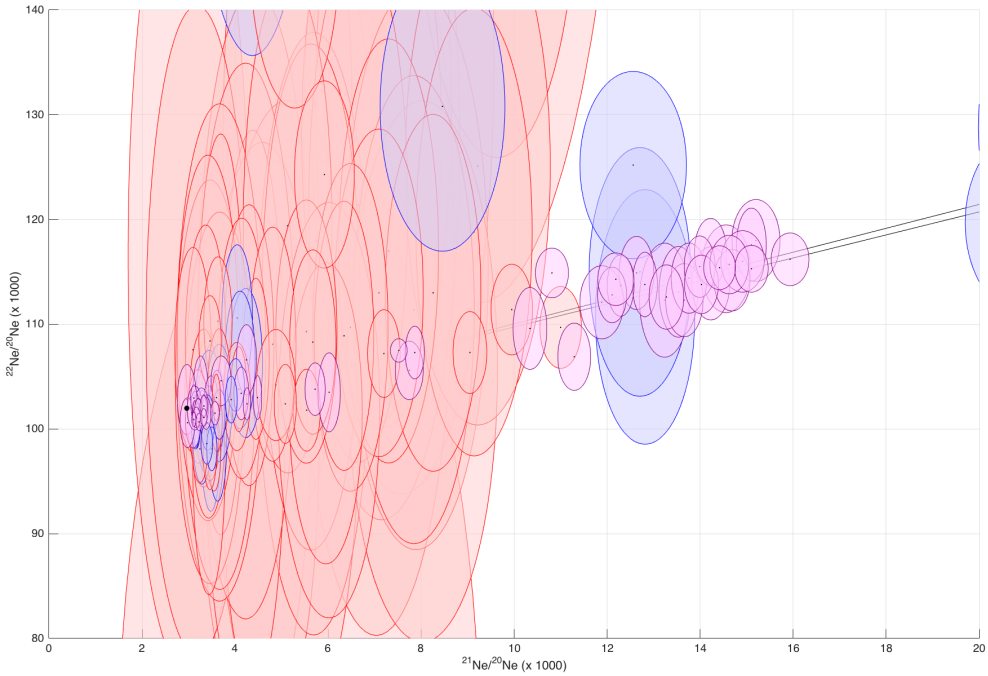
140
130
120
110
100
90
80
0
2
4
6
8
10
12
14
16
18
20
$^{22}Ne/^{20}Ne$ (x 1000)
$^{21}Ne/^{20}Ne$ (x 1000)

Supplementary Figure SF2. Ne isotope ratios measured in all heating steps for all Mackay Glacier erratic samples. Ellipses are 68% confidence regions. The black dot is the isotope composition of atmospheric Ne and the black lines show the atmospheric-cosmogenic mixing line (Niedermann, 2000; the separation of the lines reflects the uncertainty in the isotope composition of cosmogenic Ne). The color-coding reflects extraction temperature: light blue, $<$1000°C; light red, $\geq$ 1000°.

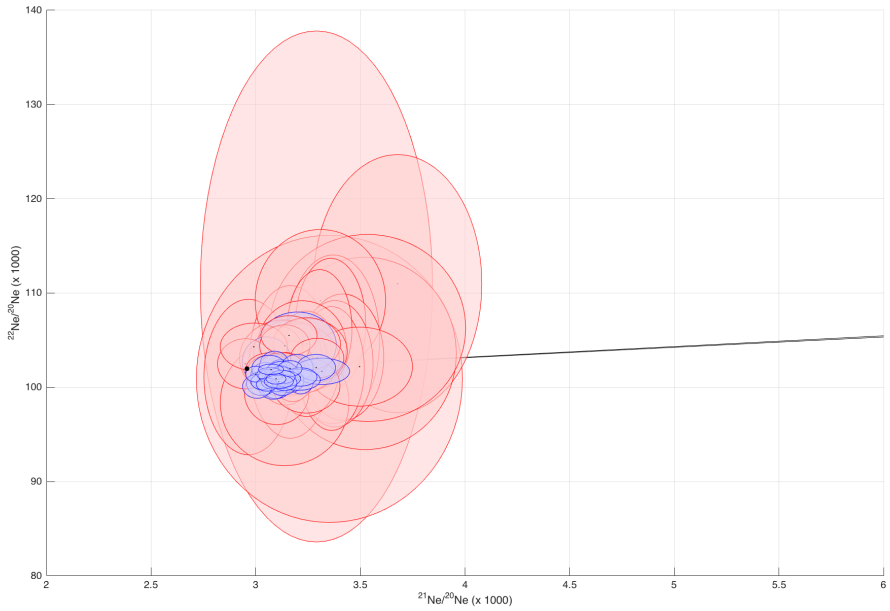

Table S1a. Complete step-degassing neon isotope measurements on Beacon Heights core samples made on BGC "MAPII" system, June-July 2010

Sample name	Aliquot	Aliquot weight (g)	Heating temperature (deg C)	Heating time (hr)	Total ^{20}Ne released[1] (10^9 atoms)	Total ^{21}Ne released[2] (10^6 atoms)	^{21}Ne / ^{20}Ne[3] (10^{-3})	^{22}Ne / ^{20}Ne[3] (10^{-3})	Excess ^{21}Ne[4] This heating step (10^6 atoms g^{-1})	Excess ^{21}Ne as % of ^{21}Ne released in this heating step	Percent of total excess ^{21}Ne released in this step	Total excess ^{21}Ne (10^6 atoms g^{-1})
001-BCO	a	0.0791	390	0.2	0.400 +/- 0.015	31.873 +/- 0.739	78.856 +/- 3.066	185.2 +/- 8.6	383.99 +/- 9.40	95	69	554.3 +/- 10.7
			780	0.2	1.101 +/- 0.013	16.540 +/- 0.443	14.912 +/- 0.333	116.0 +/- 2.1	166.33 +/- 5.08	80	30	
			1140	0.2	0.117 +/- 0.011	0.663 +/- 0.063	5.632 +/- 0.754	112.6 +/- 17.3	3.96 +/- 0.90	47	1	
	b	0.0844	370	0.17	0.498 +/- 0.014	33.284 +/- 0.584	66.895 +/- 1.965	172.3 +/- 6.3	377.10 +/- 6.97	96	68	557.5 +/- 7.9
			780	0.17	1.196 +/- 0.012	18.074 +/- 0.33	15.102 +/- 0.229	117.6 +/- 2.5	172.07 +/- 3.70	80	31	
			1140	0.17	0.208 +/- 0.011	1.321 +/- 0.068	6.343 +/- 0.457	108.9 +/- 9.2	8.35 +/- 0.89	53	1	
	c	0.0935	390	0.2	0.758 +/- 0.013	39.054 +/- 0.822	51.230 +/- 1.034	159.1 +/- 3.7	391.49 +/- 8.84	94	70	557.3 +/- 10.0
			780	0.2	1.274 +/- 0.016	18.725 +/- 0.456	14.626 +/- 0.299	115.7 +/- 2.0	158.91 +/- 4.55	79	29	
			1140	0.2	0.182 +/- 0.011	1.185 +/- 0.083	6.480 +/- 0.580	109.7 +/- 11.2	6.87 +/- 0.96	54	1	
BCO-2	a	0.0978	390	0.2	0.431 +/- 0.010	41.235 +/- 0.949	94.595 +/- 2.574	212.9 +/- 6.9	403.55 +/- 9.74	96	74	544.8 +/- 10.6
			780	0.2	1.232 +/- 0.020	17.081 +/- 0.384	13.761 +/- 0.275	114.4 +/- 2.4	136.03 +/- 3.99	78	25	
			1140	0.2	0.103 +/- 0.011	0.814 +/- 0.078	7.893 +/- 1.109	115.3 +/- 19.2	5.18 +/- 0.86	62	1	
	b	0.1113	390	0.2	0.702 +/- 0.019	44.636 +/- 0.909	63.261 +/- 1.807	175.8 +/- 5.7	380.29 +/- 8.21	95	70	540.2 +/- 9.1
			780	0.2	1.499 +/- 0.017	21.733 +/- 0.482	14.418 +/- 0.245	115.4 +/- 1.5	154.37 +/- 3.73	79	29	
			1140	0.2	0.239 +/- 0.011	1.325 +/- 0.096	5.534 +/- 0.470	109.3 +/- 9.0	5.52 +/- 0.92	46	1	
	c	0.0941	390	0.2	1.092 +/- 0.023	39.534 +/- 0.882	36.030 +/- 0.789	138.7 +/- 3.4	383.64 +/- 9.43	91	70	547.7 +/- 10.7
			780	0.2	1.365 +/- 0.025	18.700 +/- 0.45	13.661 +/- 0.288	112.3 +/- 2.5	155.28 +/- 4.86	78	28	
			1140	0.2	0.306 +/- 0.009	1.737 +/- 0.102	5.672 +/- 0.355	108.3 +/- 6.3	8.81 +/- 1.13	48	2	
	d	0.0857	390	0.2	0.882 +/- 0.015	36.050 +/- 0.811	40.665 +/- 0.781	144.4 +/- 3.2	388.06 +/- 9.51	92	71	548.4 +/- 11.0
			780	0.2	1.081 +/- 0.018	16.472 +/- 0.46	15.200 +/- 0.369	118.0 +/- 2.8	154.39 +/- 5.32	80	28	
			1140	0.2	0.274 +/- 0.011	1.319 +/- 0.088	4.807 +/- 0.359	108.1 +/- 8.0	5.90 +/- 1.17	38	1	
BCO-3	a	0.1126	390	0.2	0.532 +/- 0.018	45.327 +/- 0.914	84.138 +/- 2.879	193.6 +/- 7.6	383.69 +/- 8.17	95	71	544.1 +/- 9.1
			780	0.2	1.338 +/- 0.015	21.480 +/- 0.512	15.934 +/- 0.291	116.2 +/- 1.8	154.12 +/- 3.89	81	28	
			1140	0.2	0.113 +/- 0.011	1.050 +/- 0.083	9.217 +/- 1.117	125.1 +/- 17.7	6.30 +/- 0.79	68	1	
	b	0.098	390	0.2	0.541 +/- 0.012	39.758 +/- 0.839	73.064 +/- 1.818	177.9 +/- 5.7	387.15 +/- 8.60	95	72	540.5 +/- 9.5
			780	0.2	1.284 +/- 0.015	18.086 +/- 0.422	14.028 +/- 0.261	113.8 +/- 2.0	144.99 +/- 3.83	79	27	
			1140	0.2	0.123 +/- 0.012	1.187 +/- 0.1	9.630 +/- 1.248	154.4 +/- 20.4	8.36 +/- 1.09	69	2	
	c	0.0753	390	0.2	0.725 +/- 0.020	31.337 +/- 0.71	42.988 +/- 1.251	146.2 +/- 5.4	385.56 +/- 9.50	93	70	549.7 +/- 10.9
			780	0.2	1.142 +/- 0.020	15.492 +/- 0.394	13.534 +/- 0.300	113.1 +/- 3.1	160.37 +/- 5.30	78	29	
			1140	0.2	0.243 +/- 0.011	1.008 +/- 0.082	4.144 +/- 0.372	107.7 +/- 8.9	3.82 +/- 1.17	29	1	
BCO-4	a	0.0958	390	0.2	0.492 +/- 0.017	39.847 +/- 0.795	80.081 +/- 2.866	186.3 +/- 8.2	395.67 +/- 8.35	95	74	537.0 +/- 9.2
			780	0.2	2.790 +/- 0.017	21.175 +/- 0.526	7.520 +/- 0.128	107.5 +/- 0.8	132.85 +/- 3.82	60	25	
			1140	0.2	0.132 +/- 0.011	1.209 +/- 0.066	9.139 +/- 0.893	118.8 +/- 15.3	8.49 +/- 0.77	67	2	
	b	0.1078	390	0.2	0.504 +/- 0.013	42.354 +/- 0.84	83.646 +/- 2.278	199.6 +/- 6.8	376.94 +/- 7.83	96	72	525.9 +/- 8.7
			780	0.2	1.373 +/- 0.019	19.607 +/- 0.406	14.223 +/- 0.247	116.9 +/- 2.3	143.41 +/- 3.75	79	27	
			1140	0.2	0.201 +/- 0.012	1.202 +/- 0.091	5.953 +/- 0.559	101.5 +/- 10.3	5.59 +/- 0.91	50	1	
	c	0.0835	390	0.2	0.673 +/- 0.022	34.423 +/- 0.892	50.934 +/- 1.830	153.5 +/- 6.0	386.39 +/- 10.76	94	73	526.3 +/- 11.8
			780	0.2	0.964 +/- 0.018	14.048 +/- 0.397	14.557 +/- 0.378	115.3 +/- 3.0	133.90 +/- 4.82	80	25	
			1140	0.2	0.135 +/- 0.012	0.902 +/- 0.069	6.649 +/- 0.762	121.4 +/- 17.6	5.98 +/- 0.93	55	1	
BCO-5	a	0.1107	390	0.2	0.455 +/- 0.012	46.013 +/- 0.957	99.888 +/- 2.790	215.2 +/- 7.1	398.40 +/- 8.69	96	74	537.1 +/- 9.3
			780	0.2	1.356 +/- 0.014	19.140 +/- 0.449	13.989 +/- 0.238	115.5 +/- 2.1	135.08 +/- 3.23	78	25	
			1140	0.2	0.101 +/- 0.011	0.704 +/- 0.082	6.936 +/- 1.076	128.1 +/- 19.9	3.63 +/- 0.80	57	1	
	b	0.1316	390	0.2	0.618 +/- 0.013	51.838 +/- 1.007	83.445 +/- 1.853	193.3 +/- 5.5	377.84 +/- 7.69	96	72	527.7 +/- 8.5
			780	0.2	1.560 +/- 0.018	23.658 +/- 0.517	15.103 +/- 0.257	115.3 +/- 1.6	143.91 +/- 3.50	80	27	
			1140	0.2	0.191 +/- 0.012	1.358 +/- 0.104	7.093 +/- 0.682	113.0 +/- 11.2	5.99 +/- 0.84	58	1	

BCO-6	a	0.094	390	0.2	0.736	+/-	0.015	38.827	+/-	0.826	52.109	+/-	1.209	157.5	+/-	4.6	384.78	+/-	8.83	93	74	523.1	+/-	9.7
			780	0.2	1.199	+/-	0.015	16.069	+/-	0.397	13.275	+/-	0.267	112.6	+/-	2.2	131.54	+/-	3.80	77	25			
			1140	0.2	0.130	+/-	0.011	1.027	+/-	0.087	7.846	+/-	0.928	111.4	+/-	16.0	6.75	+/-	0.99	62	1			
	b	0.0934	390	0.2	0.520	+/-	0.014	35.103	+/-	0.741	67.182	+/-	1.923	175.3	+/-	6.1	357.42	+/-	7.98	95	69	521.7	+/-	9.1
			780	0.2	1.229	+/-	0.017	18.134	+/-	0.403	14.684	+/-	0.278	114.2	+/-	2.1	154.33	+/-	4.25	79	30			
			1140	0.2	0.175	+/-	0.011	1.453	+/-	0.094	8.258	+/-	0.736	113.0	+/-	12.2	9.95	+/-	1.07	64	2			
BCO-8	a	0.1014	390	0.2	0.694	+/-	0.014	40.874	+/-	0.866	58.197	+/-	1.338	166.1	+/-	4.4	377.90	+/-	8.59	94	74	511.4	+/-	9.1
			780	0.2	1.333	+/-	0.014	17.238	+/-	0.379	12.811	+/-	0.192	113.8	+/-	2.2	129.47	+/-	2.85	76	25			
			1140	0.2	0.135	+/-	0.011	0.817	+/-	0.084	6.019	+/-	0.781	101.8	+/-	14.2	4.06	+/-	0.89	50	1			
	b	0.0975	390	0.2	0.474	+/-	0.011	37.310	+/-	0.77	78.303	+/-	1.981	188.3	+/-	6.3	366.21	+/-	7.94	96	71	514.8	+/-	9.0
			780	0.2	1.227	+/-	0.016	17.514	+/-	0.425	14.229	+/-	0.292	113.9	+/-	2.5	141.84	+/-	4.14	79	28			
			1140	0.2	0.130	+/-	0.017	1.050	+/-	0.071	8.027	+/-	1.155	105.5	+/-	18.5	6.78	+/-	0.89	63	1			
BCO-10	a	0.0936	390	0.2	0.486	+/-	0.016	39.648	+/-	0.816	80.573	+/-	2.730	186.7	+/-	7.4	403.00	+/-	8.77	95	81	498.4	+/-	9.3
			780	0.2	1.050	+/-	0.013	11.975	+/-	0.319	11.293	+/-	0.253	106.9	+/-	2.3	93.47	+/-	3.09	73	19			
			1140	0.2	0.082	+/-	0.011	0.422	+/-	0.073	5.121	+/-	1.098	100.5	+/-	22.1	1.89	+/-	0.85	42	0			
	b	0.0777	390	0.2	0.260	+/-	0.013	29.791	+/-	0.591	114.060	+/-	5.696	232.7	+/-	14.0	371.05	+/-	7.65	97	76	487.2	+/-	9.0
			780	0.2	0.991	+/-	0.016	11.813	+/-	0.351	11.885	+/-	0.337	112.1	+/-	2.5	113.83	+/-	4.58	75	23			
			1140	0.2	0.084	+/-	0.011	0.433	+/-	0.062	5.133	+/-	0.995	127.6	+/-	26.1	2.35	+/-	0.90	42	0			
BCO-12	a	0.1273	390	0.2	0.823	+/-	0.012	48.411	+/-	0.989	58.106	+/-	0.995	169.1	+/-	3.4	356.53	+/-	7.80	94	76	466.3	+/-	8.3
			780	0.2	1.458	+/-	0.014	17.829	+/-	0.445	12.107	+/-	0.224	112.8	+/-	1.9	104.77	+/-	2.77	75	22			
			1140	0.2	0.147	+/-	0.013	1.077	+/-	0.067	7.299	+/-	0.770	117.0	+/-	14.5	5.00	+/-	0.60	59	1			
	b	0.0952	390	0.2	0.433	+/-	0.011	35.566	+/-	0.707	81.682	+/-	2.148	197.3	+/-	6.9	357.73	+/-	7.46	96	76	467.8	+/-	8.2
			780	0.2	1.055	+/-	0.015	13.372	+/-	0.322	12.632	+/-	0.267	114.9	+/-	2.5	107.24	+/-	3.35	76	23			
			1140	0.2	0.100	+/-	0.011	0.569	+/-	0.062	5.689	+/-	0.872	109.1	+/-	20.6	2.85	+/-	0.74	48	1			
BCO-18	a	0.1219	390	0.2	0.462	+/-	0.011	42.637	+/-	0.7	91.747	+/-	2.264	202.8	+/-	6.4	336.58	+/-	5.77	96	78	433.8	+/-	6.2
			780	0.2	1.230	+/-	0.011	15.238	+/-	0.317	12.290	+/-	0.206	113.7	+/-	2.1	94.18	+/-	2.24	75	22			
			1140	0.2	0.058	+/-	0.013	0.544	+/-	0.068	9.211	+/-	2.292	182.8	+/-	50.7	3.00	+/-	0.64	67	1			
	b	0.1391	390	0.2	0.439	+/-	0.009	51.931	+/-	0.823	117.094	+/-	2.559	237.5	+/-	6.5	359.80	+/-	5.94	96	83	432.5	+/-	6.4
			780	0.2	1.244	+/-	0.011	13.556	+/-	0.355	10.813	+/-	0.254	114.9	+/-	1.7	70.26	+/-	2.36	72	16			
			1140	0.2	0.073	+/-	0.010	0.562	+/-	0.071	7.582	+/-	1.420	135.0	+/-	29.5	2.43	+/-	0.55	60	1			
	c	0.1102	390	0.2	0.214	+/-	0.013	38.282	+/-	0.854	179.500	+/-	11.194	314.2	+/-	21.7	342.19	+/-	7.79	99	78	438.3	+/-	8.4
			780	0.2	1.114	+/-	0.012	13.564	+/-	0.382	12.187	+/-	0.278	114.3	+/-	1.8	93.25	+/-	2.99	76	21			
			1140	0.2	0.078	+/-	0.011	0.546	+/-	0.053	7.037	+/-	1.188	117.3	+/-	26.5	2.87	+/-	0.56	58	1			
	d	0.0538	390	0.2	0.163	+/-	0.017	18.992	+/-	0.44	115.711	+/-	12.024	219.2	+/-	25.6	340.56	+/-	8.27	96	77	442.5	+/-	9.3
			780	0.2	0.520	+/-	0.010	6.956	+/-	0.201	13.235	+/-	0.385	112.3	+/-	3.9	99.34	+/-	3.80	77	22			
			1140	0.2	0.059	+/-	0.029	0.319	+/-	0.047	5.381	+/-	2.786	67.3	+/-	42.1	2.63	+/-	1.83	44	1			
BCO-53	a	0.1267	390	0.2	0.346	+/-	0.013	25.331	+/-	0.501	72.822	+/-	2.868	183.7	+/-	9.1	190.68	+/-	3.98	95	77	247.5	+/-	4.7
			780	0.2	1.428	+/-	0.014	11.165	+/-	0.337	7.745	+/-	0.216	105.6	+/-	2.0	53.95	+/-	2.50	61	22			
			1140	0.2	0.087	+/-	0.012	0.625	+/-	0.064	7.152	+/-	1.201	127.5	+/-	25.9	2.86	+/-	0.58	58	1			
	b	0.1293	390	0.2	0.306	+/-	0.012	25.017	+/-	0.55	81.881	+/-	3.396	196.0	+/-	9.8	186.96	+/-	4.28	97	75	249.0	+/-	4.7
			780	0.2	1.551	+/-	0.016	12.188	+/-	0.306	7.864	+/-	0.148	107.3	+/-	1.8	58.83	+/-	1.88	62	24			
			1140	0.2	0.100	+/-	0.012	0.717	+/-	0.059	7.191	+/-	1.047	131.0	+/-	22.1	3.26	+/-	0.54	59	1			
BCO-83	a	0.1225	390	0.2	0.255	+/-	0.016	16.139	+/-	0.381	62.963	+/-	4.025	167.3	+/-	13.2	124.81	+/-	3.14	95	80	155.3	+/-	3.6
			780	0.2	1.180	+/-	0.015	7.171	+/-	0.214	6.022	+/-	0.172	103.5	+/-	2.7	29.49	+/-	1.70	50	19			
			1140	0.2	0.081	+/-	0.011	0.362	+/-	0.056	4.415	+/-	0.899	106.3	+/-	25.5	0.96	+/-	0.53	33	1			
	b	0.1417	390	0.2	0.293	+/-	0.011	18.216	+/-	0.479	62.074	+/-	2.484	179.8	+/-	9.1	122.32	+/-	3.40	95	82	149.2	+/-	3.7
			780	0.2	1.287	+/-	0.014	7.345	+/-	0.232	5.721	+/-	0.156	103.8	+/-	1.8	25.08	+/-	1.45	48	17			
			1140	0.2	0.121	+/-	0.012	0.619	+/-	0.059	5.130	+/-	0.682	119.4	+/-	16.9	1.85	+/-	0.48	42	1			
BCO-151	a	0.1229	390	0.2	0.276	+/-	0.016	6.099	+/-	0.197	22.000	+/-	1.446	128.8	+/-	10.7	42.70	+/-	1.66	86	77	55.5	+/-	2.1
			780	0.2	1.209	+/-	0.012	5.042	+/-	0.15	4.133	+/-	0.114	103.4	+/-	1.8	11.54	+/-	1.13	28	21			
			1140	0.2	0.093	+/-	0.010	0.432	+/-	0.069	4.585	+/-	0.874	98.6	+/-	20.6	1.23	+/-	0.61	35	2			
	b	0.1383	390	0.2	0.337	+/-	0.011	7.042	+/-	0.229	20.904	+/-	0.862	119.7	+/-	6.1	43.68	+/-	1.68	86	78	56.1	+/-	2.3
			780	0.2	1.279	+/-	0.015	5.428	+/-	0.215	4.245	+/-	0.155	106.6	+/-	2.4	11.89	+/-	1.44	30	21			
			1140	0.2	0.143	+/-	0.012	0.494	+/-	0.064	3.461	+/-	0.533	104.5	+/-	13.8	0.52	+/-	0.53	14	1			

BCO-201	b	0.139	390	0.2	0.280 +/- 0.015	3.555 +/- 0.138	12.704 +/- 0.781	115.0 +/- 8.5	19.62 +/- 1.04	77	77	25.4 +/- 1.5
			780	0.2	1.275 +/- 0.015	4.440 +/- 0.157	3.485 +/- 0.111	102.3 +/- 2.0	4.82 +/- 1.02	15	19	
			1140	0.2	0.107 +/- 0.012	0.451 +/- 0.064	4.227 +/- 0.750	108.4 +/- 19.0	0.97 +/- 0.52	30	4	
	c	0.1373	390	0.2	0.297 +/- 0.016	3.848 +/- 0.121	12.815 +/- 0.764	110.7 +/- 8.7	21.34 +/- 0.95	76	76	28.1 +/- 1.7
			780	0.2	1.252 +/- 0.011	4.671 +/- 0.213	3.701 +/- 0.156	104.6 +/- 1.7	6.77 +/- 1.43	20	24	
			1140	0.2	0.068 +/- 0.011	0.206 +/- 0.054	2.996 +/- 0.929	116.5 +/- 28.7	- +/- -	0	0	
BCO-449	a	0.1298	390	0.2	0.451 +/- 0.013	1.919 +/- 0.108	4.229 +/- 0.257	106.3 +/- 5.1	4.41 +/- 0.88	30	87	5.1 +/- 1.7
			780	0.2	1.173 +/- 0.013	3.510 +/- 0.177	2.963 +/- 0.147	102.8 +/- 2.4	0.04 +/- 1.33	0	1	
			1140	0.2	0.118 +/- 0.010	0.439 +/- 0.07	3.664 +/- 0.661	107.3 +/- 17.0	0.64 +/- 0.59	19	13	
	b	0.412	370	0.17	1.362 +/- 0.014	5.482 +/- 0.193	4.013 +/- 0.134	104.2 +/- 1.8	3.48 +/- 0.45	26	56	6.3 +/- 0.8
			780	0.17	3.908 +/- 0.031	12.445 +/- 0.268	3.161 +/- 0.059	101.4 +/- 0.9	1.92 +/- 0.56	6	31	
			1140	0.17	0.712 +/- 0.014	2.492 +/- 0.118	3.461 +/- 0.172	108.4 +/- 3.1	0.87 +/- 0.30	14	14	
BCO-860	a	0.1477	390	0.2	0.509 +/- 0.013	2.105 +/- 0.112	4.105 +/- 0.234	106.6 +/- 4.7	3.95 +/- 0.80	28	62	6.3 +/- 1.6
			780	0.2	1.571 +/- 0.015	4.971 +/- 0.194	3.134 +/- 0.117	102.0 +/- 1.5	1.86 +/- 1.24	6	29	
			1140	0.2	0.170 +/- 0.011	0.588 +/- 0.073	3.416 +/- 0.472	108.7 +/- 12.5	0.53 +/- 0.54	13	8	
	b	0.4446	390	0.2	1.948 +/- 0.024	7.707 +/- 0.195	3.917 +/- 0.092	102.8 +/- 1.6	4.20 +/- 0.41	24	48	8.8 +/- 0.8
			780	0.2	4.520 +/- 0.038	15.190 +/- 0.334	3.329 +/- 0.059	102.2 +/- 0.7	3.76 +/- 0.60	11	43	
			1140	0.2	0.525 +/- 0.008	1.935 +/- 0.091	3.659 +/- 0.173	104.4 +/- 3.7	0.83 +/- 0.20	19	9	
BCO-998	a	0.1493	390	0.2	0.745 +/- 0.014	2.480 +/- 0.1	3.288 +/- 0.138	99.2 +/- 3.2	1.64 +/- 0.69	10	64	2.6 +/- 1.5
			780	0.2	1.545 +/- 0.016	4.649 +/- 0.185	2.976 +/- 0.114	100.6 +/- 1.7	0.18 +/- 1.19	1	7	
			1140	0.2	0.155 +/- 0.011	0.578 +/- 0.075	3.668 +/- 0.535	102.7 +/- 12.9	0.74 +/- 0.56	19	29	
	b	0.4544	390	0.2	2.423 +/- 0.026	8.299 +/- 0.239	3.392 +/- 0.090	98.6 +/- 1.4	2.31 +/- 0.48	13	30	7.6 +/- 0.8
			780	0.2	4.918 +/- 0.042	16.520 +/- 0.322	3.327 +/- 0.048	101.1 +/- 0.6	3.98 +/- 0.52	11	52	
			1140	0.2	0.566 +/- 0.012	2.302 +/- 0.116	4.038 +/- 0.210	103.1 +/- 3.7	1.34 +/- 0.26	27	18	
BCO-1300	a	0.1455	390	0.2	0.601 +/- 0.013	2.226 +/- 0.116	3.660 +/- 0.201	102.5 +/- 4.0	2.90 +/- 0.84	19	67	4.3 +/- 1.5
			780	0.2	1.441 +/- 0.016	4.522 +/- 0.18	3.101 +/- 0.119	100.7 +/- 1.8	1.41 +/- 1.19	5	33	
			1140	0.2	0.092 +/- 0.011	0.296 +/- 0.064	3.179 +/- 0.784	109.4 +/- 22.2	- +/- -		0	
	b	0.409	390	0.2	1.984 +/- 0.023	7.338 +/- 0.222	3.662 +/- 0.105	101.4 +/- 1.7	3.41 +/- 0.51	19	61	5.6 +/- 0.9
			780	0.2	4.214 +/- 0.035	13.349 +/- 0.315	3.137 +/- 0.062	102.2 +/- 1.0	1.83 +/- 0.64	6	33	
			1140	0.2	0.434 +/- 0.014	1.452 +/- 0.091	3.324 +/- 0.228	102.0 +/- 5.4	0.39 +/- 0.24	11	7	
BCO-1784	a	0.1531	390	0.2	0.567 +/- 0.012	1.976 +/- 0.128	3.444 +/- 0.230	101.5 +/- 4.3	1.80 +/- 0.86	14	23	7.9 +/- 1.4
			780	0.2	1.990 +/- 0.016	6.803 +/- 0.178	3.378 +/- 0.076	101.5 +/- 1.1	5.45 +/- 1.00	12	69	
			1140	0.2	0.257 +/- 0.011	0.883 +/- 0.073	3.368 +/- 0.312	108.3 +/- 8.0	0.69 +/- 0.53	12	9	
	b	0.4619	390	0.2	2.482 +/- 0.025	8.773 +/- 0.224	3.499 +/- 0.081	98.1 +/- 1.5	2.90 +/- 0.44	15	42	6.9 +/- 0.9
			780	0.2	5.977 +/- 0.053	19.381 +/- 0.431	3.211 +/- 0.059	101.8 +/- 0.8	3.26 +/- 0.77	8	47	
			1140	0.2	1.201 +/- 0.017	3.925 +/- 0.149	3.242 +/- 0.120	98.1 +/- 2.3	0.74 +/- 0.31	9	11	
BCO-2520	a	0.154	390	0.2	0.430 +/- 0.013	1.758 +/- 0.091	4.045 +/- 0.236	110.6 +/- 5.0	3.03 +/- 0.64	27	36	8.5 +/- 1.5
			780	0.2	1.789 +/- 0.014	5.934 +/- 0.212	3.277 +/- 0.109	102.1 +/- 1.3	3.69 +/- 1.27	10	44	
			1140	0.2	0.201 +/- 0.010	0.879 +/- 0.066	4.301 +/- 0.382	108.0 +/- 9.6	1.75 +/- 0.47	31	21	
	b	0.4436	390	0.2	1.568 +/- 0.023	5.371 +/- 0.186	3.410 +/- 0.105	100.6 +/- 1.9	1.59 +/- 0.37	13	35	4.5 +/- 0.9
			780	0.2	5.300 +/- 0.048	16.816 +/- 0.457	3.169 +/- 0.059	101.1 +/- 0.7	2.51 +/- 0.71	7	55	
			1140	0.2	0.809 +/- 0.017	2.598 +/- 0.135	3.203 +/- 0.164	101.2 +/- 3.2	0.45 +/- 0.30	8	10	

Notes:

[1] Computed by comparison to ^{20}Ne signal in air pipettes. 1-sigma uncertainty includes measurement uncertainty of ^{20}Ne signal in this analysis and the reproducibility of the air pipette signal

[2] Computed by comparison to ^{21}Ne signal in air pipettes. 1-sigma uncertainty includes measurement uncertainty of ^{21}Ne signal in this analysis and the reproducibility of the air pipette signal

[3] Isotope ratio measured internally during each analysis: does not involve normalization to the Ne isotope signals in the air pipettes.

[4] Analyses where cosmogenic ^{21}Ne was not distinguishable from zero at 1 sigma are not shown. Excess ^{21}Ne concentrations were calculated by normalization to either the ^{20}Ne or ^{21}Ne signal in the air pipettes, depending on which method yielded better precision.

Table S1b: Complete step-degassing neon isotope measurements made at CRPG.

Sample name	Aliquot	Aliquot weight (g)	Grain size (mm)	Heating temperature (deg C)	Heating time (hr)	Total ^{20}Ne released (10^{9} atoms)	Total ^{21}Ne released (10^{6} atoms)	^{21}Ne / ^{20}Ne (10^{-3})	^{22}Ne / ^{20}Ne (10^{-3})	Excess ^{21}Ne This heating step (10^{6} atoms g^{-1})	Excess ^{21}Ne as % of ^{21}Ne released in this heating step	Percent of total excess ^{21}Ne released in this step	Total excess ^{21}Ne (10^{6} atoms g^{-1})
BHC-A (17-18 cm)	a	0.1518	0.5-1	800	0.4	7.09 +/- 0.13	73.3 +/- 1.2	10.34 +/- 0.26	109.6 +/- 2.8	345 +/- 14	72	85	403 +/- 14
				1220	1.4	1.231 +/- 0.025	12.24 +/- 0.31	9.95 +/- 0.32	111.4 +/- 3.1	56.7 +/- 2.8	71	14	
				1260	2.4	0.0602 +/- 0.0067	0.494 +/- 0.059	8.2 +/- 1.3	13.7 +/- 11.9	2.08 +/- 0.58	64	1	
BHC-B (31-32 cm)	a	0.0992	0.5-2	400	0.4	0.2180 +/- 0.0078	2.74 +/- 0.15	12.56 +/- 0.82	125.2 +/- 6.4	21.1 +/- 2.0	77	6	342 +/- 14
				1250	0.4	3.926 +/- 0.074	43.29 +/- 0.93	11.0 +/- 0.32	109.7 +/- 2.8	319 +/- 14	73	93	
				1340	0.4	0.0287 +/- 0.0066	0.232 +/- 0.052	8.1 +/- 2.6	244 +/- 61	1.48 +/- 0.83	64	0	
BHC-C (51-52 cm)	a	0.0824	0.5-2	400	0.4	0.1272 +/- 0.0070	1.08 +/- 0.11	8.46 +/- 0.96	130.8 +/- 9.9	8.5 +/- 1.6	65	4	239 +/- 11
				1260	0.4	3.125 +/- 0.060	28.26 +/- 0.61	9.05 +/- 0.26	107.3 +/- 2.8	231 +/- 11	68	96	
BHC-D (81-82 cm)	a	0.0441	0.5-1	400	0.4	-0.0033 +/- 0.0065	0.290 +/- 0.060	-	-	<DL[1]			174 +/- 11
				1250	0.4	1.805 +/- 0.035	13.00 +/- 0.38	7.20 +/- 0.25	107.2 +/- 3.0	174 +/- 11	59	100	
BHC-E (101-102 cm)	a	0.0387	0.5-1	400	0.4	-0.0042 +/- 0.0065	-0.029 +/- 0.041	7 +/- 15	-	<DL			119 +/- 10
				1270	0.4	1.780 +/- 0.035	9.85 +/- 0.31	5.54 +/- 0.21	101.8 +/- 2.8	118.5 +/- 9.8	47	100	
BHC-F (152-153 cm)	a	0.1133	0.5-1	1200	0.4	2.905 +/- 0.056	14.75 +/- 0.41	5.08 +/- 0.17	102.4 +/- 2.7	54.3 +/- 4.5	42	100	54.3 +/- 4.5
				1280	0.4	0.0003 +/- 0.0065	0.001 +/- 0.040	4 +/- 156	-	<DL			
BHC-G (202-203 cm)	a	0.0525	0.5-2	800	0.4	1.950 +/- 0.038	7.04 +/- 0.18	3.61 +/- 0.12	101.7 +/- 2.8	24.2 +/- 4.3	18	57	42.7 +/- 5.2
				1220	0.4	0.504 +/- 0.012	2.46 +/- 0.14	4.88 +/- 0.30	104.2 +/- 3.8	18.5 +/- 2.9	40	43	
BHC-I (335-336 cm)	a	0.1088	0.5-1	800	0.4	4.363 +/- 0.085	14.22 +/- 0.42	3.26 +/- 0.12	103.2 +/- 2.7	12.1 +/- 4.6	9	68	17.7 +/- 4.7
				1220	0.4	0.2076 +/- 0.0078	1.229 +/- 0.084	5.92 +/- 0.46	124.3 +/- 6.4	5.65 +/- 0.91	50	32	
BHC-J (448-449 cm)	a	0.1129	0.5-2	1250	0.4	4.214 +/- 0.080	14.60 +/- 0.32	3.46 +/- 0.10	97.7 +/- 2.5	18.9 +/- 3.8	15	100	18.9 +/- 3.8
BHC-M (996-998 cm)	a	0.0837	0.2-0.5	400	0.4	0.0852 +/- 0.0067	0.372 +/- 0.061	4.37 +/- 0.80	158 +/- 16	1.44 +/- 0.82	32	6	22.4 +/- 4.7
				1270	0.4	2.938 +/- 0.056	10.16 +/- 0.32	3.46 +/- 0.13	98.7 +/- 2.6	17.5 +/- 4.5	14	78	
				1400	0.4	0.1248 +/- 0.0071	0.659 +/- 0.078	5.28 +/- 0.69	146 +/- 11	3.5 +/- 1.1	44	15	
BHC-P (2518-2520 cm)	a	0.2072	0.2-1	1250	0.4	4.373 +/- 0.086	15.53 +/- 0.34	3.55 +/- 0.10	97.7 +/- 2.6	12.5 +/- 2.2	17	100	12.5 +/- 2.2

Notes:

[1] Below detection limit

Table S1c: Complete step-degassing neon isotope results for replicate Ne-21 measurements made on the BGC "MAPII" system of samples prepared at CRPG.

Sample name	Aliquot	Aliquot weight (g)	Heating temperature (deg C)	Heating time (hr)	Total ^{20}Ne released[1] (10^9 atoms)	Total ^{21}Ne released[2] (10^6 atoms)	^{21}Ne / ^{20}Ne[3] (10^{-3})	^{22}Ne / ^{20}Ne[3] (10^{-3})	Excess ^{21}Ne This heating step (10^6 atoms g^{-1})	Excess ^{21}Ne as % of ^{21}Ne released in this heating step	Percent of total excess ^{21}Ne released in this step	Total excess ^{21}Ne (10^6 atoms g^{-1})
BHC-CRPG-152	a	0.1538	390	0.2	2.580 +/- 0.100	9.177 +/- 0.177	3.624 +/- 0.140	98.7 +/- 4.0	11.15 +/- 2.24	19	18	63.0 +/- 3.2
			780	0.2	4.302 +/- 0.096	19.186 +/- 0.356	4.483 +/- 0.065	103.0 +/- 1.5	42.63 +/- 2.06	34	68	
			1140	0.2	1.269 +/- 0.024	5.103 +/- 0.18	4.080 +/- 0.122	103.8 +/- 2.9	9.25 +/- 1.02	28	15	
BHC-CRPG-152	b	0.118	390	0.2	1.615 +/- 0.069	5.541 +/- 0.144	3.478 +/- 0.162	100.1 +/- 5.7	7.10 +/- 2.13	15	11	63.1 +/- 3.4
			780	0.2	3.820 +/- 0.039	16.072 +/- 0.247	4.256 +/- 0.056	102.4 +/- 1.1	41.98 +/- 1.87	31	67	
			1140	0.2	1.108 +/- 0.045	4.857 +/- 0.168	4.447 +/- 0.205	106.7 +/- 5.5	13.98 +/- 1.82	34	22	
BHC-CRPG-448	a	0.2708	390	0.2	5.274 +/- 0.105	16.318 +/- 0.331	3.147 +/- 0.066	100.6 +/- 1.8	3.66 +/- 1.29	6	22	16.7 +/- 2.0
			780	0.2	10.570 +/- 0.227	32.753 +/- 0.544	3.114 +/- 0.031	100.9 +/- 0.5	6.05 +/- 1.24	5	36	
			1140	0.2	2.905 +/- 0.065	10.326 +/- 0.281	3.607 +/- 0.083	100.8 +/- 2.1	6.95 +/- 0.91	18	42	
BHC-CRPG-2518	a	0.3279	390	0.2	4.683 +/- 0.097	14.649 +/- 0.251	3.175 +/- 0.062	101.1 +/- 2.1	3.08 +/- 0.89	7	21	15.0 +/- 1.6
			780	0.2	11.584 +/- 0.117	35.947 +/- 0.476	3.133 +/- 0.033	101.6 +/- 0.8	6.15 +/- 1.17	6	41	
			1140	0.2	2.964 +/- 0.051	10.504 +/- 0.281	3.597 +/- 0.063	103.0 +/- 1.6	5.77 +/- 0.58	18	38	

[1] Computed by comparison to ^{20}Ne signal in air pipettes. 1-sigma uncertainty includes measurement uncertainty of ^{20}Ne signal in this analysis and the reproducibility of the air pipette signal

[2] Computed by comparison to ^{21}Ne signal in air pipettes. 1-sigma uncertainty includes measurement uncertainty of ^{21}Ne signal in this analysis and the reproducibility of the air pipette signal

[3] Isotope ratio measured internally during each analysis: does not involve normalization to the Ne isotope signals in the air pipettes.

Table S1d: Complete step-degassing neon isotope measurements made on the BGC "Ohio" system in 2017.

Sample name	Aliquot	Aliquot weight (g)	Heating temperature (deg C)	Heating time (hr)	Total ^{20}Ne released[1] (10^8 atoms)	Total ^{21}Ne released[2] (10^6 atoms)	Total ^{22}Ne released[3] (10^8 atoms)	^{21}Ne / ^{20}Ne[4] (10^{-3})	^{22}Ne / ^{20}Ne[4] (10^{-3})	Excess ^{21}Ne This heating step (10^8 atoms g^{-1})	Excess ^{21}Ne as % of ^{21}Ne released in this heating step	Percent of total excess ^{21}Ne released in this step	Total excess ^{21}Ne (10^8 atoms g^{-1})
BCO247	b	0.1689	850	0.25	6.354 +/- 0.062	21.148 +/- 0.458	649.203 +/- 8.965	3.328 +/- 0.038	102.2 +/- 0.8	13.89 +/- 1.48	11	93	15.0 +/- 1.6
			1200	0.25	0.259 +/- 0.015	0.955 +/- 0.077	28.218 +/- 3.265	3.690 +/- 0.348	109.0 +/- 13.7	1.12 +/- 0.52	20	7	
	c	0.1234	850	0.25	4.161 +/- 0.062	14.846 +/- 0.328	422.354 +/- 6.363	3.568 +/- 0.067	101.5 +/- 0.8	20.54 +/- 2.29	17	94	21.8 +/- 2.4
			1200	0.25	0.336 +/- 0.010	1.152 +/- 0.079	33.210 +/- 1.675	3.431 +/- 0.242	98.9 +/- 5.3	1.28 +/- 0.66	14	6	
BCO447	b	0.1447	850	0.25	4.150 +/- 0.042	12.920 +/- 0.31	427.294 +/- 6.166	3.113 +/- 0.048	103.0 +/- 0.9	4.42 +/- 1.42	5	71	6.2 +/- 1.5
			1200	0.25	0.186 +/- 0.015	0.813 +/- 0.072	18.942 +/- 3.278	4.378 +/- 0.500	102.0 +/- 19.0	1.82 +/- 0.58	32	29	
	c	0.1535	850	0.25	3.970 +/- 0.058	12.737 +/- 0.262	404.596 +/- 6.094	3.208 +/- 0.053	101.9 +/- 0.7	6.45 +/- 1.41	8	97	6.7 +/- 1.5
			1200	0.25	0.238 +/- 0.008	0.737 +/- 0.066	25.610 +/- 1.600	3.095 +/- 0.281	107.6 +/- 7.0	0.21 +/- 0.44	4	3	
BCO613	b	0.1604	850	0.25	5.990 +/- 0.058	18.886 +/- 0.438	608.369 +/- 8.457	3.153 +/- 0.044	101.6 +/- 0.8	7.24 +/- 1.70	6	86	8.4 +/- 1.8
			1200	0.25	0.394 +/- 0.016	1.353 +/- 0.088	38.087 +/- 3.281	3.438 +/- 0.248	96.8 +/- 9.0	1.17 +/- 0.60	14	14	
	c	0.1645	850	0.25	6.167 +/- 0.091	19.896 +/- 0.378	620.837 +/- 9.098	3.226 +/- 0.048	100.7 +/- 0.6	10.02 +/- 1.83	8	85	11.8 +/- 1.9
			1200	0.25	0.426 +/- 0.010	1.547 +/- 0.093	46.974 +/- 1.883	3.632 +/- 0.218	110.3 +/- 4.4	1.74 +/- 0.57	19	18	

[1] Computed by comparison to ^{20}Ne signal in air pipettes. 1-sigma uncertainty includes measurement uncertainty of ^{20}Ne signal in this analysis and the reproducibility of the air pipette signal
[2] Computed by comparison to ^{21}Ne signal in air pipettes. 1-sigma uncertainty includes measurement uncertainty of ^{21}Ne signal in this analysis and the reproducibility of the air pipette signal
[3] Computed by comparison to ^{22}Ne signal in air pipettes. 1-sigma uncertainty includes measurement uncertainty of ^{21}Ne signal in this analysis and the reproducibility of the air pipette signal
[4] Isotope ratio measured internally during each analysis: does not involve normalization to the Ne isotope signals in the air pipettes.

Table S3. Complete step-degassing neon isotope measurements on erratics of Beacon Sandstone from Mackay Glacier, BGC "Ohio" system, 2017-18.
Note: aliquots of CRONUS-A run at the same time as these analyses yielded 320.1 +/- 6.8 Matoms/g cosmogenic ^{21}Ne (mean and standard deviation of 15 measurements). Thus, no correction is required to normalize these results to the consensus value for CRONUS-A.

Sample name	Aliquot	Aliquot weight (g)	Heating temperature (deg C)	Heating time (hr)	Total ^{20}Ne released[1] (10^9 atoms)	Total ^{21}Ne released[2] (10^6 atoms)	Total ^{22}Ne released[3] (10^6 atoms)	^{21}Ne / ^{20}Ne[4] (10^{-3})	^{22}Ne / ^{20}Ne[4] (10^{-3})	Excess ^{21}Ne This heating step (10^6 atoms g^{-1})	Excess ^{21}Ne as % of ^{21}Ne released in this heating step	Percent of total excess ^{21}Ne released in this heating step	Total excess ^{21}Ne (10^6 atoms g^{-1})
GR47	a	0.1281	800	0.25	5.1132 +/- 0.0696	16.908 +/- 0.443	522.284 +/- 6.686	3.289 +/- 0.066	102.1 +/- 1	13.19 +/- 2.64	10	92	14.34 +/- 2.99
			1100	0.25	0.8187 +/- 0.0158	2.597 +/- 0.186	80.496 +/- 3.988	3.138 +/- 0.22	98.4 +/- 4.8	1.15 +/- 1.41	6	8	
	b	0.1612	800	0.25	6.5392 +/- 0.0728	20.821 +/- 0.61	664.973 +/- 9.872	3.1 +/- 0.044	101 +/- 0.7	5.72 +/- 1.79	4	82	6.97 +/- 2.04
			1100	0.25	1.4242 +/- 0.0217	4.52 +/- 0.196	142.092 +/- 3.614	3.1 +/- 0.11	99.4 +/- 2.4	1.25 +/- 0.97	4	18	
	c	0.1558	800	0.25	6.2638 +/- 0.0907	19.683 +/- 0.393	629.115 +/- 9.086	3.11 +/- 0.05	100.6 +/- 0.5	6.08 +/- 2	5	100	6.08 +/- 2.00
			1100	0.25	1.2783 +/- 0.0229	3.791 +/- 0.129	130.615 +/- 2.933	2.95 +/- 0.095	102.5 +/- 1.9	-0.07 +/- 0.78	0	-1	
GR48	a	0.1345	800	0.25	1.8703 +/- 0.0289	6.016 +/- 0.269	195.39 +/- 4.791	3.199 +/- 0.133	104.5 +/- 2.5	3.34 +/- 1.85	7	100	3.34 +/- 1.85
			1100	0.25	0.3416 +/- 0.0108	1.158 +/- 0.157	34.408 +/- 3.708	3.352 +/- 0.455	100.9 +/- 10.9	1 +/- 1.15	12	30	
	b	0.1469	800	0.25	1.8387 +/- 0.0261	5.766 +/- 0.211	190.075 +/- 3.985	3.053 +/- 0.084	102.7 +/- 1.9	1.18 +/- 1.05	3	41	2.85 +/- 1.22
			1100	0.25	0.3414 +/- 0.0164	1.286 +/- 0.089	38.017 +/- 3	3.678 +/- 0.288	111 +/- 9.8	1.67 +/- 0.63	19	59	
GR51	a	0.1345	800	0.25	7.456 +/- 0.1074	22.54 +/- 0.521	745.818 +/- 8.547	3.007 +/- 0.05	100.1 +/- 0.9	2.66 +/- 2.78	2	50	5.28 +/- 3.31
			1100	0.25	1.558 +/- 0.0241	5.017 +/- 0.255	160.28 +/- 4.323	3.184 +/- 0.154	103 +/- 2.7	2.62 +/- 1.79	7	50	
	b	0.1432	800	0.25	7.3138 +/- 0.1252	22.351 +/- 0.534	732.899 +/- 11.262	3.053 +/- 0.036	100.3 +/- 0.5	4.8 +/- 1.83	3	69	6.95 +/- 2.10
			1100	0.25	1.8453 +/- 0.0335	5.778 +/- 0.188	188.011 +/- 3.562	3.125 +/- 0.079	102 +/- 1.2	2.15 +/- 1.03	5	31	
GR52	a	0.1482	800	0.25	4.4173 +/- 0.0504	14.812 +/- 0.483	444.212 +/- 5.343	3.316 +/- 0.095	101.7 +/- 1	10.66 +/- 2.85	11	87	12.21 +/- 3.15
			1100	0.25	1.3032 +/- 0.0181	4.12 +/- 0.21	132.614 +/- 3.794	3.135 +/- 0.152	103.1 +/- 2.9	1.55 +/- 1.34	6	13	
	b	0.1453	800	0.25	4.8671 +/- 0.087	15.656 +/- 0.427	491.262 +/- 7.983	3.213 +/- 0.057	101.1 +/- 0.7	8.52 +/- 1.92	8	79	10.72 +/- 2.12
			1100	0.25	1.1193 +/- 0.0212	3.639 +/- 0.149	116.923 +/- 2.722	3.244 +/- 0.115	104.6 +/- 2	2.2 +/- 0.89	9	21	
GR53B	a	0.1604	800	0.25	5.3 +/- 0.0593	17.137 +/- 0.391	534.8 +/- 6.412	3.198 +/- 0.055	102.1 +/- 1	7.93 +/- 1.83	7	80	9.9 +/- 2.16
			1100	0.25	0.5469 +/- 0.0118	1.949 +/- 0.187	57.381 +/- 3.833	3.535 +/- 0.335	106.3 +/- 7.1	1.97 +/- 1.14	16	20	
	b	0.1519	800	0.25	4.8506 +/- 0.0848	15.369 +/- 0.377	493.967 +/- 8.07	3.164 +/- 0.041	102 +/- 0.6	6.57 +/- 1.3	6	89	7.4 +/- 1.40
			1100	0.25	0.3614 +/- 0.0116	1.199 +/- 0.079	39.422 +/- 1.79	3.309 +/- 0.223	109.2 +/- 5.4	0.83 +/- 0.52	11	11	
GR54	a	0.1437	800	0.25	5.724 +/- 0.0645	17.915 +/- 0.4	566.88 +/- 6.853	3.097 +/- 0.052	100.2 +/- 1	5.5 +/- 2.06	4	61	8.95 +/- 2.61
			1100	0.25	1.7045 +/- 0.0228	5.555 +/- 0.248	174.753 +/- 4.495	3.249 +/- 0.135	103.8 +/- 2.5	3.45 +/- 1.6	9	39	
	b	0.1572	800	0.25	6.4785 +/- 0.1133	20.285 +/- 0.511	654.142 +/- 10.493	3.127 +/- 0.044	101.1 +/- 0.5	6.93 +/- 1.82	5	70	9.86 +/- 1.98
			1100	0.25	1.3701 +/- 0.0257	4.524 +/- 0.153	141.141 +/- 2.845	3.294 +/- 0.091	103.1 +/- 1.5	2.93 +/- 0.79	10	30	
GR56	a	0.1639	800	0.25	6.0705 +/- 0.0688	19.168 +/- 0.447	608.739 +/- 6.491	3.125 +/- 0.056	101.5 +/- 0.9	6.17 +/- 2.09	5	59	10.48 +/- 2.54
			1100	0.25	1.3102 +/- 0.018	4.593 +/- 0.249	132.395 +/- 4.178	3.496 +/- 0.181	102.2 +/- 3	4.31 +/- 1.45	15	41	
	b	0.1748	800	0.25	6.473 +/- 0.1128	20.334 +/- 0.508	649.933 +/- 10.589	3.137 +/- 0.043	100.5 +/- 0.6	6.6 +/- 1.6	6	80	8.22 +/- 1.73
			1100	0.25	0.996 +/- 0.0193	3.238 +/- 0.131	99.679 +/- 2.476	3.242 +/- 0.115	100.2 +/- 2.1	1.62 +/- 0.65	9	20	
	c	0.1538	800	0.25	5.8184 +/- 0.061	18.64 +/- 0.301	590.352 +/- 7.489	3.122 +/- 0.033	101.1 +/- 0.9	6.17 +/- 1.26	5	86	7.21 +/- 1.45
			1100	0.25	0.774 +/- 0.0093	2.5 +/- 0.113	79.467 +/- 4.54	3.165 +/- 0.141	102.7 +/- 5.8	1.04 +/- 0.71	6	14	
	d	0.1428	800	0.25	5.3939 +/- 0.0547	17.307 +/- 0.348	543.364 +/- 7.049	3.127 +/- 0.049	100.4 +/- 0.9	6.37 +/- 1.87	5	69	9.19 +/- 2.06
			1100	0.25	0.9565 +/- 0.0114	3.298 +/- 0.13	98.073 +/- 4.632	3.379 +/- 0.13	102.5 +/- 4.8	2.82 +/- 0.87	12	31	
	e	0.1333	800	0.25	5.3157 +/- 0.0753	16.496 +/- 0.462	534.726 +/- 9.642	3.027 +/- 0.051	100.4 +/- 0.9	2.72 +/- 2.02	2	100	2.72 +/- 2.02
			1100	0.25	0.7322 +/- 0.0126	2.228 +/- 0.124	74.509 +/- 4.503	2.965 +/- 0.152	101.1 +/- 5.9	0.03 +/- 0.84	0	1	
	f	0.1146	800	0.25	4.8351 +/- 0.0699	15.198 +/- 0.453	494.517 +/- 9.099	3.065 +/- 0.06	102 +/- 1	4.5 +/- 2.55	3	65	6.96 +/- 2.72
			1100	0.25	0.6849 +/- 0.0127	2.368 +/- 0.121	72.428 +/- 4.528	3.37 +/- 0.159	105.1 +/- 6.4	2.46 +/- 0.95	12	35	
GR59	a	0.1477	800	0.25	6.1714 +/- 0.071	19.971 +/- 0.567	613.974 +/- 6.66	3.204 +/- 0.075	100.8 +/- 0.8	10.25 +/- 3.16	8	83	12.33 +/- 3.38
			1100	0.25	1.1655 +/- 0.0175	3.764 +/- 0.185	120.161 +/- 4.213	3.221 +/- 0.152	104.3 +/- 3.5	2.08 +/- 1.2	8	17	
	b	0.1587	800	0.25	6.7033 +/- 0.12	20.933 +/- 0.492	679.103 +/- 10.682	3.118 +/- 0.036	101.4 +/- 0.6	6.72 +/- 1.53	5	97	6.96 +/- 1.75
			1100	0.25	1.1815 +/- 0.0222	3.544 +/- 0.153	123.117 +/- 2.698	2.991 +/- 0.115	104.3 +/- 1.8	0.24 +/- 0.85	1	3	
	c	0.1527	800	0.25	6.3355 +/- 0.0912	20.029 +/- 0.366	640.009 +/- 9.642	3.129 +/- 0.043	101.2 +/- 0.7	7.08 +/- 1.79	5	100	7.08 +/- 1.79
			1100	0.25	1.3532 +/- 0.0228	4.27 +/- 0.129	140.768 +/- 2.98	3.139 +/- 0.086	104.4 +/- 1.6	1.6 +/- 0.76	6	23	
	d	0.1237	800	0.25	5.8285 +/- 0.083	18.535 +/- 0.481	589.461 +/- 10.612	3.101 +/- 0.04	100.8 +/- 0.9	6.69 +/- 1.91	4	67	9.99 +/- 2.16
			1100	0.25	0.8916 +/- 0.0146	3.123 +/- 0.145	92.664 +/- 4.541	3.416 +/- 0.14	103.2 +/- 4.8	3.3 +/- 1.01	13	33	
GR62B	b	0.1521	800	0.25	6.5887 +/- 0.1145	20.282 +/- 0.512	670.901 +/- 10.552	3.073 +/- 0.043	101.9 +/- 0.4	4.95 +/- 1.89	4	82	6.07 +/- 2.08
			1100	0.25	1.6417 +/- 0.0303	5.043 +/- 0.168	166.868 +/- 3.261	3.063 +/- 0.081	101.7 +/- 1.4	1.12 +/- 0.88	3	18	
	c	0.1662	800	0.25	6.8795 +/- 0.0983	21.318 +/- 0.405	695.942 +/- 10.17	3.068 +/- 0.045	101.4 +/- 0.5	4.52 +/- 1.86	4	74	6.13 +/- 2.02
			1100	0.25	1.4922 +/- 0.025	4.706 +/- 0.143	151.18 +/- 3.044	3.138 +/- 0.087	101.6 +/- 1.5	1.61 +/- 0.78	6	26	

GR64	b	0.176	800	0.25	11.4659 +/- 0.1893	35.472 +/- 0.735	1160.3 +/- 19.927	3.097 +/- 0.034	100.9 +/- 0.4	9.01 +/- 2.21	4	87	10.32 +/- 2.41
			1100	0.25	2.0134 +/- 0.0347	6.2 +/- 0.204	205.468 +/- 4.196	3.073 +/- 0.084	101.5 +/- 1.4	1.31 +/- 0.96	4	13	
	c	0.1623	800	0.25	9.8631 +/- 0.1	30.343 +/- 0.509	1002.681 +/- 10.832	2.999 +/- 0.034	101.4 +/- 0.6	2.45 +/- 2.08	1	48	5.13 +/- 2.32
			1100	0.25	1.7626 +/- 0.0157	5.763 +/- 0.18	181.723 +/- 4.945	3.205 +/- 0.095	103.2 +/- 2.7	2.68 +/- 1.03	8	52	
	d	0.1605	800	0.25	9.954 +/- 0.1006	31.333 +/- 0.508	1005.154 +/- 11.189	3.07 +/- 0.032	100.7 +/- 0.6	6.87 +/- 2.01	4	72	9.6 +/- 2.23
			1100	0.25	2.0164 +/- 0.0173	6.534 +/- 0.172	204.843 +/- 4.943	3.176 +/- 0.077	101.7 +/- 2.3	2.73 +/- 0.97	7	28	
	e	0.1614	800	0.25	10.2585 +/- 0.1457	32.14 +/- 0.783	1041.771 +/- 17.303	3.054 +/- 0.029	101.2 +/- 0.5	6.06 +/- 1.85	3	67	8.99 +/- 2.02
			1100	0.25	1.8442 +/- 0.0277	6.08 +/- 0.192	191.857 +/- 5.504	3.215 +/- 0.072	103.3 +/- 2.5	2.93 +/- 0.82	8	33	
	f	0.1314	800	0.25	8.3114 +/- 0.1179	25.846 +/- 0.67	839.648 +/- 14.261	3.031 +/- 0.039	100.6 +/- 0.6	4.56 +/- 2.48	2	70	6.51 +/- 2.74
			1100	0.25	1.4087 +/- 0.0147	4.509 +/- 0.167	145.6 +/- 4.889	3.141 +/- 0.108	102.6 +/- 3.2	1.95 +/- 1.16	6	30	
GR67	b	0.1402	800	0.25	3.7346 +/- 0.0637	11.505 +/- 0.268	374.451 +/- 6.856	3.083 +/- 0.049	100 +/- 0.9	3.32 +/- 1.3	4	77	4.31 +/- 1.40
			1100	0.25	0.2449 +/- 0.0089	0.865 +/- 0.074	25.509 +/- 1.692	3.524 +/- 0.311	103.6 +/- 7.3	0.99 +/- 0.53	16	23	
	c	0.1324	800	0.25	4.2004 +/- 0.0603	13.447 +/- 0.37	427.765 +/- 8.267	3.12 +/- 0.05	101.4 +/- 1.1	5.11 +/- 1.59	5	100	5.11 +/- 1.59
			1100	0.25	0.2163 +/- 0.0066	0.726 +/- 0.086	24.131 +/- 4.256	3.29 +/- 0.397	110.7 +/- 19.4	0.54 +/- 0.65	10	11	
CC90	b	0.1585	800	0.25	5.2237 +/- 0.0862	16.414 +/- 0.388	528.466 +/- 9.353	3.145 +/- 0.049	100.9 +/- 0.6	6.13 +/- 1.63	6	83	7.4 +/- 1.78
			1100	0.25	1.3504 +/- 0.0248	4.209 +/- 0.135	140.759 +/- 3.391	3.108 +/- 0.084	103.7 +/- 2	1.27 +/- 0.71	5	17	
	c	0.1456	800	0.25	4.8246 +/- 0.0692	15.918 +/- 0.419	488.326 +/- 9.002	3.215 +/- 0.044	100.7 +/- 1	8.5 +/- 1.47	8	77	11.05 +/- 1.63
			1100	0.25	0.9183 +/- 0.0104	3.157 +/- 0.112	94.407 +/- 4.483	3.362 +/- 0.112	102 +/- 4.7	2.55 +/- 0.7	12	23	
	d	0.1383	800	0.25	4.5563 +/- 0.0657	14.604 +/- 0.394	462.325 +/- 8.697	3.123 +/- 0.047	101 +/- 1.1	5.42 +/- 1.54	5	68	8.02 +/- 1.72
			1100	0.25	0.8978 +/- 0.011	3.087 +/- 0.115	96.571 +/- 4.704	3.358 +/- 0.12	106.7 +/- 5	2.6 +/- 0.77	12	32	
CC95	b	0.1614	800	0.25	5.4887 +/- 0.0954	17.288 +/- 0.408	555.048 +/- 9.894	3.16 +/- 0.05	100.7 +/- 0.9	6.86 +/- 1.69	6	79	8.68 +/- 1.90
			1100	0.25	1.4641 +/- 0.0274	4.641 +/- 0.162	155.229 +/- 3.061	3.159 +/- 0.096	105.5 +/- 1.5	1.82 +/- 0.87	6	21	
	c	0.134	800	0.25	4.4464 +/- 0.0636	14.1 +/- 0.393	457.06 +/- 8.65	3.09 +/- 0.051	102.3 +/- 1.1	4.35 +/- 1.69	4	63	6.9 +/- 1.87
			1100	0.25	0.9861 +/- 0.0113	3.341 +/- 0.119	105.572 +/- 4.708	3.305 +/- 0.111	106.2 +/- 4.5	2.55 +/- 0.81	10	37	
	d	0.139	800	0.25	4.8531 +/- 0.0704	15.171 +/- 0.425	493.522 +/- 9.265	3.046 +/- 0.051	101.1 +/- 1.1	3.04 +/- 1.79	3	58	5.24 +/- 1.99
			1100	0.25	1.0766 +/- 0.0116	3.584 +/- 0.133	111.281 +/- 4.62	3.243 +/- 0.113	102.5 +/- 4	2.2 +/- 0.88	9	42	

[1] Computed by comparison to ^{20}Ne signal in air pipettes. 1-sigma uncertainty includes measurement uncertainty of ^{20}Ne signal in this analysis and the reproducibility of the air pipette signal
[2] Computed by comparison to ^{21}Ne signal in air pipettes. 1-sigma uncertainty includes measurement uncertainty of ^{21}Ne signal in this analysis and the reproducibility of the air pipette signal
[3] Computed by comparison to ^{22}Ne signal in air pipettes. 1-sigma uncertainty includes measurement uncertainty of ^{21}Ne signal in this analysis and the reproducibility of the air pipette signal
[4] Isotope ratio measured internally during each analysis: does not involve normalization to the Ne isotope signals in the air pipettes.

Table S4. Uranium and thorium concentrations in quartz samples.

Sample	Mass (mg)	Lab	[U] (ppm)	Average	St. Dev.	% St. Dev.	[Th] (ppm)	Average	St. Dev.	% St. Dev.
Core samples (depths in cm)										
0-1.4	3.1	Caltech	0.0816	0.0835	0.0027	3	0.3753	0.3657	0.0136	4
	194.1	BGC	0.0854				0.3560			
2-3	3.5	Caltech	0.0826	0.0799	0.0037	5	0.4650	0.4508	0.0201	4
	214.6	BGC	0.0773				0.4365			
3-4	3.5	Caltech	0.1079	0.1085	0.0009	1	0.4106	0.3979	0.0180	5
	193.8	BGC	0.1091				0.3852			
4-5	3.4	Caltech	0.0731	0.0800	0.0098	12	0.2297	0.2437	0.0199	8
	228.4	BGC	0.0869				0.2578			
5-6	3.4	Caltech	0.2399	0.2580	0.0256	10	0.5030	0.4781	0.0352	7
	218.3	BGC	0.2761				0.4532			
6-7	3.4	Caltech	0.0727	0.0730	0.0004	1	0.4121	0.3741	0.0538	14
	231.0	BGC	0.0733				0.3360			
8-9	3.4	Caltech	0.0693	0.0695	0.0003	0.4	0.2780	0.2722	0.0083	3
	238.0	BGC	0.0697				0.2664			
10-11	3.2	Caltech	0.0998	0.0845	0.0216	26	0.2927	0.2771	0.0220	8
	233.3	BGC	0.0692				0.2616			
12-13	3.5	Caltech	0.0454	0.0434	0.0028	6	0.2443	0.2200	0.0345	16
	225.9	BGC	0.0415				0.1956			
17-18		CRPG	0.7260	0.7260			1.2790	1.2790		
18-19	3.1	Caltech	0.2780	0.2680	0.0142	5	2.1794	1.8239	0.5029	28
	43.8	BGC	0.2580				1.4683			
31-32		CRPG	0.4590	0.4590			1.3320	1.3320		
51-52		CRPG	0.2400	0.2400			0.5220	0.5220		
53-54	3.5	Caltech	0.0884	0.0882	0.0003	0	0.3389	0.3473	0.0117	3
	202.7	BGC	0.0880				0.3556			
81-82		CRPG	0.3890	0.3890			0.8460	0.8460		
83-84	3.2	Caltech	0.0690	0.0665	0.0035	5	0.4495	0.3626	0.1230	34
	226.2	BGC	0.0640				0.2756			
101-102		CRPG	0.3360	0.3360			0.8590	0.8590		
151-152	3.1	Caltech	0.0482	0.0592	0.0156	26	0.4334	0.3262	0.1517	47
	238.7	BGC	0.0702				0.2189			
152-153		CRPG	0.3340	0.2883	0.0646	22	1.0050	0.8172	0.2656	33
	198.7	BGC	0.2426				0.6293			
201-202	3.4	Caltech	0.2315	0.1707	0.0860	50	1.2666	0.8179	0.6345	78
	220.6	BGC	0.1098				0.3693			
202-203		CRPG	0.5290	0.5290			1.0340	1.0340		
247-248	87.4	BGC	0.0800	0.0800			0.2717	0.2717		
335-336		CRPG	0.4640	0.4640			0.9660	0.9660		
447-448	159.4	BGC	0.0914	0.0914			0.2678	0.2678		
448-449		CRPG	0.3480	0.3480			2.3750	2.3750		
449-451	3.1	Caltech	0.1078	0.0916	0.0228	25	0.4675	0.3567	0.1567	44
	207.4	BGC	0.0755				0.2459			
613-614	161.7	BGC	0.1039	0.1039			0.2603	0.2603		
860-862	3.3	Caltech	0.0794	0.0994	0.0213	21	0.4280	0.3987	0.0861	22
	6.0	Caltech	0.0971				0.4664			
	210.4	BGC	0.1217				0.3018			
996-998		CRPG	0.2720	0.2720			0.8710	0.8710		
998-1000	3.3	Caltech	0.0832	0.0739	0.0111	15	0.3657	0.3784	0.1177	31
	5.6	Caltech	0.0770				0.5019			
	234.8	BGC	0.0616				0.2675			
1300-1302	3.1	Caltech	0.0964	0.0963	0.0419	43	0.3610	0.2474	0.1039	42
	5.5	Caltech	0.1381				0.2239			
	225.3	BGC	0.0544				0.1573			
1784-1786	3.4	Caltech	0.0696	0.0876	0.0157	18	0.2340	0.2432	0.0101	4
	4.6	Caltech	0.0982				0.2414			
	207.9	BGC	0.0949				0.2540			
2518-2520		CRPG	0.3690	0.3570	0.0170	5	1.0380	0.7820	0.3620	46
	246.1	BGC	0.3449				0.5260			
2520-2522	3.2	Caltech	0.0729	0.0898	0.0215	24	0.3359	0.4185	0.2091	50
	6.1	Caltech	0.1140				0.6563			
	207.2	BGC	0.0824				0.2633			
Mackay Glacier sandstone erratics										

GR47	265.2	BGC	0.0846	0.0846			0.3437	0.3437		
GR48	296.8	BGC	0.0510	0.0510			0.2011	0.2011		
GR51	235.9	BGC	0.0997	0.0997			0.2859	0.2859		
GR52	269.8	BGC	0.1390	0.1390			0.2052	0.2052		
GR53b	271.8	BGC	0.1155	0.1155			0.2379	0.2379		
GR54	278.6	BGC	0.2312	0.1752	0.0792	45.2	0.2406	0.1982	0.0600	30.3
	316.8	BGC	0.1192				0.1558			
GR56	235.9	BGC	0.2387	0.2103	0.0401	19.1	0.8110	0.5052	0.4324	85.6
	310.8	BGC	0.1819				0.1995			
GR59	209.5	BGC	0.1367	0.1367			0.3446	0.3446		
GR62b	229.8	BGC	0.0938	0.0938			0.2206	0.2206		
GR64	229.3	BGC	0.1880	0.1842	0.0462	25.1	0.4537	0.4575	0.1510	33.0
	210.6	BGC	0.1363				0.3084			
	314.5	BGC	0.2284				0.6104			
GR67	311.9	BGC	0.1001	0.1001			0.1861	0.1861		
CC90	315.9	BGC	0.1531	0.1531			0.2015	0.2015		
CC95	296.0	BGC	0.1616	0.1616			0.3302	0.3302		